**ORIGINAL PAPER**

# Fluid evolution, metal source, and ore genesis of sulfide mineralization, Nim Ka Thana Copper Belt, Rajasthan, India: evidence from mineral chemistry, fluid inclusions and sulfur isotope geochemistry

Arindam Gantait[1] · Sanjoy Debnath[1] · Abhishek Anand[2] · Sukesh Jakhar[2]

## Abstract

Nim Ka Thana Copper Belt, in Rajasthan, India is well-known for the bornite dominated copper deposits. The present study area covers three prospects, i.e., Nanagwas, Dariba North, and Toda-Ramliyas, located in the central to the southern part of the belt. The sulfide mineralization is hosted within the carbonaceous phyllite and banded impure marble of the Paleo-proterozoic sequence of the Delhi Supergroup but copper mineralization is only hosted within the banded impure marble. In this study, we use mineral chemistry of sulfide minerals, fluid inclusion of quartz vein, and sulfur isotopic geochemistry to decipher the genesis of sulfide mineralization. Nim Ka Thana copper belt exhibits a wide range of Ca-Na–K-B metaso-matism. Mineral chemistry of pyrite and pyrrhotite shows Co/Ni ratio varies between 0.20–20 and 0.19–15 respectively. Three types of fluid inclusions are observed within mineralized quartz veins and homogenized within the temperature range of 121.5 °C to 390.1 °C and salinities of 0.33 wt% to 16.80 wt% NaCl equivalents. The homogenization temperature and salinity indicates the isothermal mixing and simple cooling of the ore-forming fluids and they are of metamorphic origin. Sulfur isotopic composition of major sulfides shows a bimodal distribution of $\delta^{34}S_{VCDT}$ (‰) values ranging from $-37.85‰$ to $+6.33‰$. It indicates that the ore-forming metals and sulfur come from a mixed source that encompasses sedimentary and hydrothermal sources. Based on field observation, ore mineral chemistry, petrographic study, fluid inclusion, and sulfur isotope study, it is inferred that the sulfide mineralization is overprinting of sedimentary and hydrothermal origin but copper mineralization is formed by the hydrothermal process.

**Keywords** Nim Ka Thana copper belt · Fluid inclusion · Sulfur isotope · Mineral chemistry · Bornite

✉ Arindam Gantait
agantait.gsi@gmail.com

Sanjoy Debnath
sanju.presi14@gmail.com

Abhishek Anand
abhi.tec13@gmail.com

Sukesh Jakhar
sukeshjakhar@gmail.com

1 Geological Survey of India, Western Region, Khanij Bhavan, 15-16, Jhalana Doongri, Jaipur 302004, India

2 Geological Survey of India, State Unit: Rajasthan, Khanij Bhavan, 15-16, Jhalana Doongri, Jaipur 302004, India

## Introduction

Copper is a nonferrous base metal with an average concentration of around 50 ppm in the Earth's crust. It is a transitional chalcophile element with the affinity to unite with sulfur, oxygen, and many other elements to form minerals. Major copper-bearing minerals are chalcopyrite, bornite, chalcocite, covelite, and cuprite. These minerals can originate from the different geological processes such as magmatic, sedimentary, volcanic, and hydrothermal. The majority of the world's copper ore comes from porphyry type copper deposits (Sinclair 2007; Sillitoe 2010; Sun et al. 2017) followed by sediment hosted (Hitzman et al. 2005, 2010; Borg et al. 2012; Sillitoe et al. 2017) and IOCG type of deposits (Hitzman 2000; Sillitoe 2003; Skirrow et. al. 2007; Groves et al. 2010; Sillitoe 2012).

In India, copper deposits occur in three major belts namely (1) hydrothermal type Singhbhum Copper Belt in Jharkhand comprise the Surda, Raka, and Mosaboni areas (Mishra et al. 2003; Pal et al. 2009, 2010; Chowdhury et al. 2020; Patel et al. 2021), (2) porphyry type Malanjkhand Copper deposit in Madhya Pradesh (Bhargava and Pal 2000; Stein et al. 2004; Panigrahi et al. 2009; Asthana et al. 2015), and (3) IOCG type Khetri Copper Belt in Rajasthan (Knight et al. 2002; Chen et al. 2015; Baidya et al. 2017; Li et al. 2018; Baidya and Pal 2020). These copper deposits comprise primary sulfides dominated by chalcopyrite. The most abundant ore mineral observed in most copper deposits is chalcopyrite, although bornite can be found in hypogene or supergene environments, along with various secondary sulfides (Rieger et al. 2010; Cook et al. 2011; Zhao et al. 2014; Reich and Vasconcelos 2015; Salama et al. 2016; Li et al. 2019). Chalcocite mostly occurs in the supergene environments but sometimes also occurs with hypogene conditions (Perello et al. 2001; Valencia et al. 2008; Mathur et al. 2012, 2018; Dill 2015). In India, bornite dominated copper deposits are rare. The bornite dominated linear copper deposit explored by the Geological Survey of India during the last two decades in the southeast of Khetri Copper Belt is known as Nim Ka Thana Copper Belt. Bornite is the major primary ore of copper along with chalcopyrite and chalcocite (Mukhopadhyay 2014; Sharma et al. 2015). Significant blocks explored in this area include Dokan north block, Dokan block, Baniwala Ki Dhani block, Nanagwas block, Dariba block, and the southernmost Toda-Ramliyas block (Sharma et al. 2015). Various genetic models were proposed for this bornite dominated copper deposits. Mukhopadhyay (2014) proposed sediment hosted stratiform copper deposition model for this belt and later on Mukhopadhyay et al. (2019) worked on the Bhudoli-Basari prospect and also supported this genetic model for this copper belt. Whereas Sharma et al. (2015, 2018) and Mondal et al. (2019) recorded that the mineralization is formed mainly by sedimentary process and partly by epigenetic process. Sharma et al. (2020) suggested affiliation of mineralization of Nim Ka Thana belt with a hydrothermal system akin to IOCG clan.

Ore deposits are the product of crustal evolution in specific areas and at particular stages. Hence, a full understanding of the local geological setting is a prerequisite in studying the genesis of ore deposits (Hedenquist and Lowenstern 1994; Simmons and Brown 2006; Zhu et al. 2007; Hou et al. 2008; Baker et al. 2010). Hydrothermal deposits are very significant on a global scale, although magmatic and supergene deposits are locally important. The genesis of the deposits is closely related to the geological environments including pressure and temperature conditions, and the nature/source of the hydrothermal fluid (Roedder 1984; Wilkinson 2001; Heinrich 2007). Fluid inclusion studies

have become more important in the study of ore genesis and exploration because various types of mineral deposits have different fluid characteristics, such as fluid composition, temperature, density, and gas nature. Fluid inclusions are recognized as valuable tool for mineral prospecting because of the change in these characteristics (Kesler et al. 1986; Moon 1991; Moncada et al. 2012; Xu et al. 2016; Ni et al. 2018; Liu et al. 2019). One key source of information comes from the interpretation of fluid inclusion analyses, which is vital to understanding in key changes in character of the deposit (Bodnar et al. 2014; Hedenquist and Richards 1998; Kouzmanov and Pokrovski 2012; Landtwing et al. 2010; Lecumberri-Sanchez et al. 2015; Mernagha et al. 2020). Sulfur isotope is a diverse tool that enables a detailed understanding of source rock, mineralizing fluids, altered rock, and ore deposits (Ault and Williams-Jones 2004; Seal 2006; Simons and Repley 2011; Hutchison et al. 2020). Sulfur isotope variations in ore deposition systems are very complex and best understood in the context of the total geological framework of the ore deposits and in conjunction with fluid inclusion study.

In this contribution, detailed studies on the petrography of the host rock and ore minerals, mineral chemistry of ore minerals using EPMA, fluid inclusion of mineralized quartz veins, and sulfur isotopic ratio of major ore minerals were carried out from Palaeoproterozoic Nim Ka Thana Copper Belt within the North Delhi Fold Belt, Western India, with an aim to decipher the probable mineral system of copper mineralization. An attempt has been made (i) to understand the possible source of copper bearing minerals, (ii) to characterize the ore bearing fluids, and (iii) to decipher the genesis of copper mineralization. In this paper, we present mineral chemistry, detailed fluid inclusion petrography, and microthermometry of mineralized quartz veins, the sulfur isotopic ratio of major ore minerals to decipher the genesis of copper mineralization. The result from our study has a definite bearing on the metallogenetic significance in this region and for copper mineralization systems of the world and will through light on exploration targets in allied prospects.

# Geological background

## Regional geology

The Northwestern Indian shield is represented by 3.3–2.5 Ga Archean basement known as Banded Gneissic Complex (BGC) and is overlain by 2.2–1.85 Ga Paleoproterozoic cover sequence of Aravalli-Delhi Fold Belt (Gupta 1934; Heron 1953; Gopalan et al. 1990; Wiedenbeck and Goswami 1994; Roy and Kröner 1996; Wiedenbeck et al. 1996; Golani et al. 2002; Kaur et al. 2009, 2011; Roy et al. 2012;

Fareeduddin and Banerjee 2019) (Fig. 1). The BGC is in tectonic contact with, or unconformably overlain by, two Proterozoic supracrustal sequences, the Aravalli and Delhi Supergroups (Roy et al. 1993). The Aravalli Supergroup is widely distributed in the eastern and southeastern parts of the Aravalli–Delhi Fold Belt along a NE–SW trending basin. Geochronological studies showed that Aravalli sedimentation spanned the time interval from ~ 2.3 to ~ 1.6 Ga (Ahmad et al. 2008; McKenzie et al. 2013). The Delhi Supergroup is represented by three groups—the basal Raialo Group (association of carbonates, argillites, and mafic to felsic volcanics), followed by the Alwar Group (dominantly conglomerate—quartzite association) in the middle and the Ajabgarh Group (represented by carbonates, psammo-pelite, tuff, and chert breccia) at the top (Heron 1953; Sarkar and Dasgupta 1980; Singh 1988; Roy and Jakhar 2002). These rocks overlie the pre-Delhi basement rocks of the Archaean age (Choudhary et al. 1984) with faulted contacts. The Delhi Supergroup is divided into two fold belts one is North Delhi Fold Belt (NDFB) and the other is South Delhi Fold Belt (SDFB) (Sinha Roy 1984). The North Delhi Fold Belt is thought to have formed as a process of intra-continental rifting, which resulted in mafic and felsic magmatism (Singh 1988; Sinha Roy 2004; Bhattacharya and Bull 2010). The depositional ages of the NDFB is well constrained to younger than 1.8–1.7 Ga, provided by cross cutting relationship of intrusive igneous rocks and detrital zircon age data, respectively (Biju-Sekhar et al. 2003; Kaur et al. 2007, 2009, 2011). The North Delhi Fold Belt hosts a succession of metasediments, comprising the quartzite dominated the Alwar Group and the schist and carbonate dominated the Ajabgarh Group. The rocks of the area have undergone greenschist to amphibolite facies of metamorphism with the development of garnet and staurolite within the metapelite sequence (Lal and Ackermand 1981; Naha et al. 1988; Gupta et al. 1998; Kaur et al. 2017). The North Delhi Fold Belt has been divided into three main sedimentary domains. From east to west (Singh 1988), these are the Bayana-Lalsot, the Alwar, and the Khetri sub-basins. The Khetri sub basin is popularly known as the Khetri Copper Belt hosting world class IOCG type of copper deposit (Knight et al. 2002; Chen et al. 2015; Baidya et al. 2017; Li et al. 2018). South east part of the Khetri Copper Belt, copper-bearing lithounits of Nim Ka Thana Copper Belt (NKTCB) are exposed in 30-km-long linear belt within NDFB.

Nim Ka Thana Copper Belt (NKTCB) forms the northwestern part of the North Delhi Fold Belt. NKTCB is a long 30-km copper-rich belt extended from Golwa–Gangutana (Haryana) in the north to Toda-Ramliyawas (Rajasthan) in the south and it comprises rocks which belong to the Alwar and the Ajabgarh Group (Fig. 2). The Alwar Group is represented by arenaceous facies rocks of the Pratapgarh Formation. Quartzite of the Pratapgarh Formation is massive

and at places gritty to pebbly in nature. The Pratapgarh Formation is overlain by the Kushalgarh Formation of the Ajabgarh Group. The Kushalgarh Formation is represented by calcareous packages with carbonaceous phyllite and various types of schist. Calcareous package of the Kushalgarh Formation is the host rock of copper mineralization in the NKTCB. Calcareous packages of the Kushalgarh Formation is composed of banded impure marble, dolomitic marble, and different variant of marble, which are exposed at Pancho Kharkhara, Mino Ka Nangal, Dokan, Baniwala Ki Dhani, Nathuwala, Nanagwas, Dariba, Plashwala, Toda, and Ramliyawas areas. Post Delhi intrusive granites are exposed at Dabla, Jaitpura, and Kalakhera areas. Numerous quartz, calcite, and quartz-calcite veins are also seen in the area. General strike of the lithounits of the area is NNE-SSW with steep dips toward WNW or ESE. The rocks of the area have undergone three phases of deformation. In this area, copper mineralization is mainly hosted by the calcareous rocks of Kushalgarh Formation and mineralization mostly associated with the second phases of deformation.

## Local geology and mineralization

The present study is confined to the central and southern parts of the Nim Ka Thana Copper Belt (NKTCB) of Rajasthan, India. The study area comprises three prospects, i.e., Nanagwas prospect, Dariba North prospect, and Toda-Ramliyawas prospect. Nanagwas prospect is located in the central part of the belt and Toda prospect is located in the southern part of the belt. Dariba North prospect is located in between these two prospects.

Rocks of the Kushalgrah Formation of the Ajabgarh Group of the Delhi Supergroup are exposed in the area. Major lithologies of the area are banded impure dolomitic marble, carbon phyllite, ferruginised breccia, quartzite, and younger intrusives. The sulfide mineralization is observed within the banded impure marble and carbonaceous phyllite. Copper mineralization in these prospects is mainly hosted by banded impure marble. The carbonaceous phyllite is devoid of copper mineralization.

The banded impure dolomitic marble is composed of thin alternate light and dark bands (Fig. 3a). Light colored bands are composed mainly of carbonate minerals and dark bands composed of biotite and amphibole. The light colored calcareous bands at places are siliceous in nature and stand out as ridges. The thickness of the bands varies from few millimeters to about 0.5 m. At places, laths of tremolite and actinolite are observed as clusters. Garnet and amphibole-rich zones are observed, which are associated with the mineralized zones (Fig. 3b). Rotation of garnet porphyroblast is also observed within the garnet rich zone in the banded impure marble. Scapolite clusters are also observed in proximity to the mineralized zones in the banded impure marble.
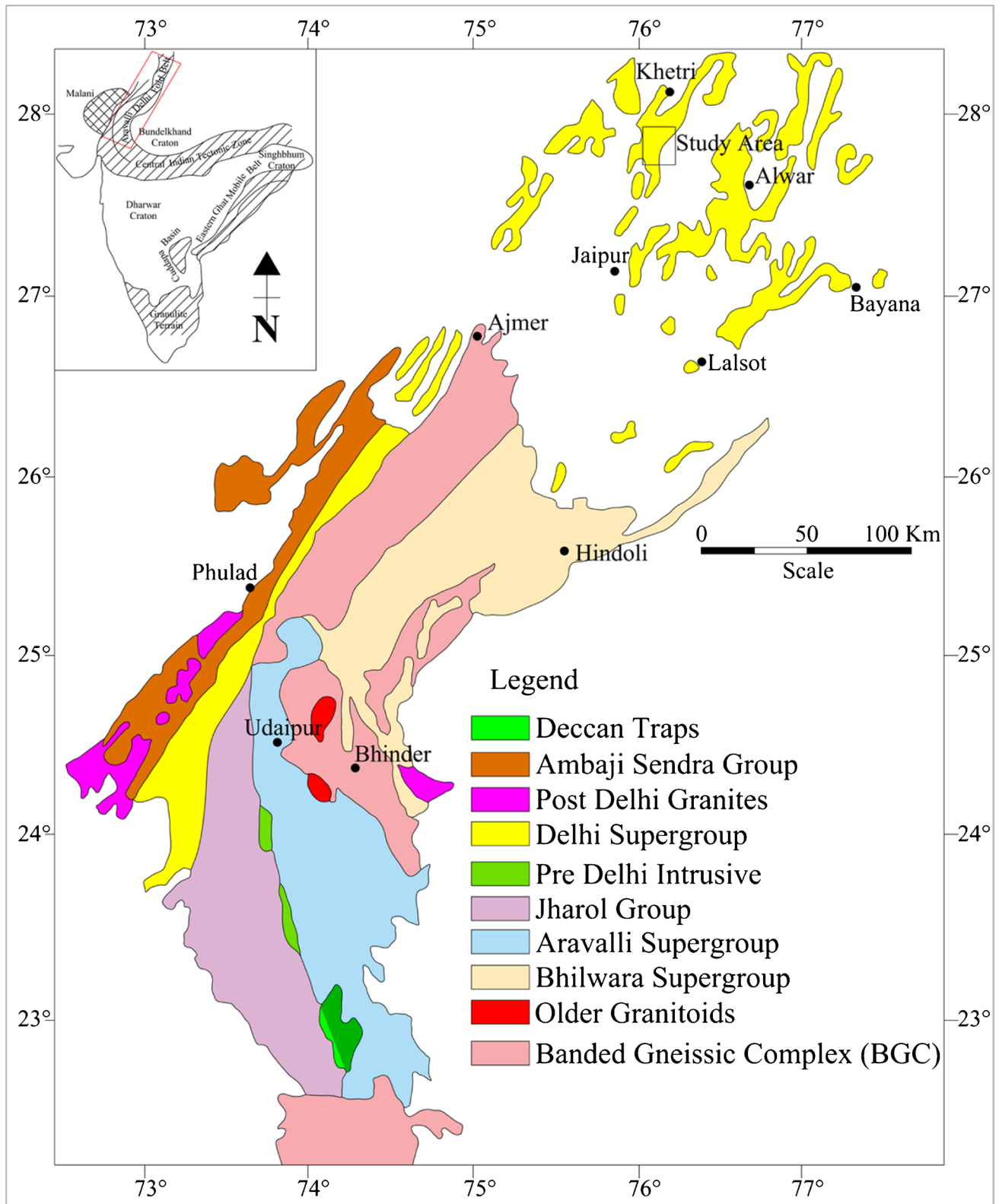
**Fig. 1** Geological map of the Aravalli-Delhi Fold Belt (after Roy 1988; Roy and Jakhar 2002). The study area (marked by black box), part of the North Delhi Fold Belt, is located in the northeastern part of the belt. Map in inset shows the locations of the Proterozoic fold belts in India and the location of the Aravalli-Delhi Fold Belt (marked by red box)

Carbonaceous phyllite unit is mostly unexposed in the study area and it forms low lying land. It is observed only in the drill core samples (Fig. 3c). This rock unit is fine to medium grained, soft, and black. This rock unit is foliated, fractured, and jointed. Foliation parallel pyrite mineralization is observed within the carbonaceous phyllite. Ferruginised breccia unit is exposed in Dariba North prospect. It is buff colored and composed of quartzite fragments within ferruginised matrix (Fig. 3d). Quartzite is massive, jointed, thickly bedded, and feldspathic in nature. Iron bands are observed within quartzite at places. Cross cutting quartz, quartz-calcite veins are observed in all the lithounits (Fig. 3e).

In NKTCB, all the lithounits show N-S to NNE-SSW structural trends with moderate to steep dips toward W to WNW. Three distinct phases of deformation are identified in the area. $D_1$ phase deformation is identified by $F_1$ isoclinal folds (Fig. 3f); $D_2$ phase deformation is marked by symmetrical to asymmetrical, tight to open inclined, moderately to steeply plunging $F_2$ folds. $F_2$ folds are profusely and pervasively developed in the area. Axial plane of $F_2$ folds are slightly inclined and trending in N-S direction and are vertical to sub-vertical. Western limb of the $F_2$ fold is overturned in the area. Several sinistral folds (S shaped) on the western limb, dextral folds (Z shaped) on the eastern limb, and M-W folds in the hinge zone are well preserved. Overall, the area exhibits an antiformal syncline and synformal anticline which have a plunge of 40° toward S35°W on mesoscopic scale. Eye-shaped $F_2$ folds showing plunge of about 50° toward S40°W have also been recorded from the western limb. Open folds and broad warps with widely spaced fracture cleavage formed during the $D_3$ phase of deformation. The axial plane of $F_3$ fold is trending E-W with vertical to steep dip toward north/south. In Dariba North prospect and Toda–Ramliyawas prospect, a N-S trending shear zone is observed. N-S trending fault present in the area which is identified by brecciation and silicification. A numbers of cross faults are observed across the strike of the lithounits. These faults strike NW–SE and dip at a high to moderate angle toward NE. These cross faults also affect the ore body in the area. The mineral assemblages of different lithounits indicate that the study area had suffered greenschist to upper amphibolite facies of metamorphism.

The Nanagwas, Dariba North, and Toda–Ramliyawas prospect consist of 3, 2, and 4 copper ore bodies having cumulative strike length of 1888 m, 900 m, and 1210 m respectively (Mondal et al. 2016; Debnath et al. 2017; Gantait et al. 2018). The width of the ore lodes vary from 2 to 40 m and plunges to SW. The grade of the copper in these prospects varies from 0.21 to 1.00%. Hydrothermal alteration viz., scapolitization, amphibolization, biotization, and tourmalinization are observed in the close proximity to the ore body (Mondal et al. 2016; Debnath et al. 2017; Gantait et al. 2018; Anand 2019). Few Pb–Zn zones are observed in Nanagwas and Dariba prospects. They are separately associated with the copper ore body and occur near to the faulted contact. In plain view, ore bodies are lenticular to irregular in shape. In cross-section view, ore bodies are in lensoidal pattern and steeply plunging toward west (Fig. 4). The ore bodies in these prospects are structurally controlled and associated with the $D_2$ phase of deformation.

## Hydrothermal alteration

Hydrothermal alteration related to copper mineralization in NKTCB is seen as Ca-Na-B-K metasomatism. Clusters of acicular actinolite and tremolite crystals within the mineralized zones represent the amphibolization. Na metasomatism is represented by the presence of soda-rich scapolite within the mineralized zones. Presence of tourmaline within sulfide zones indicates boron metasomatism in the area. Alteration of feldspar to sericite is also observed within the host rock. Silicification, chloritization, and ferruginised breccia are also observed throughout the host rock. Potassic alteration of the copper deposit is indicated by the enrichment of biotite within the mineralized zone. Propylitic alteration is represented by actinolite-chlorite assemblages.

## Nature and control of mineralization

Surface evidences of mineralization in NKTCB include few deep old workings near Baleshwar, slag heaps, and mine debris at places. Apart from these, other prominent evidences are profuse malachite staining associated with the host lithology and presence of sulfides, such as chalcopyrite, bornite, covellite, chalcocite, pyrite, and pyrrhotite associated with calcareous package of the Ajabgarh Group of the Delhi Supergroup of rock (Fig. 3g, h). Along with these ore minerals at places, barite veins is also observed in banded impure marble. Old workings for barite are also present in this area. The main ore minerals for copper are bornite, chalcopyrite, chalcocite, and covellite while other minor ore minerals such as digenite, cubanite, and djurleite are also observed. Nature of mineralization was studied in detail from borehole drill cores and as well as from the exposed host lithologies. Sulfide mineralization mainly occurs in the form of disseminated pyrite within carbonaceous phyllite and vein filled, patchy, stringers, semi-massive, and disseminated type copper ores within the banded impure marble. These ore minerals also occur as vein filling within quartz and calcite veins, fracture fills, and sometimes vug filled coarse crystals observed in borehole drill cores (Fig. 5a–i). In a few occasions chalcopyrite, bornite and chalcocite are occurring along the primary foliation and bedding i.e. parallel to $S_0$//$S_1$ planes.
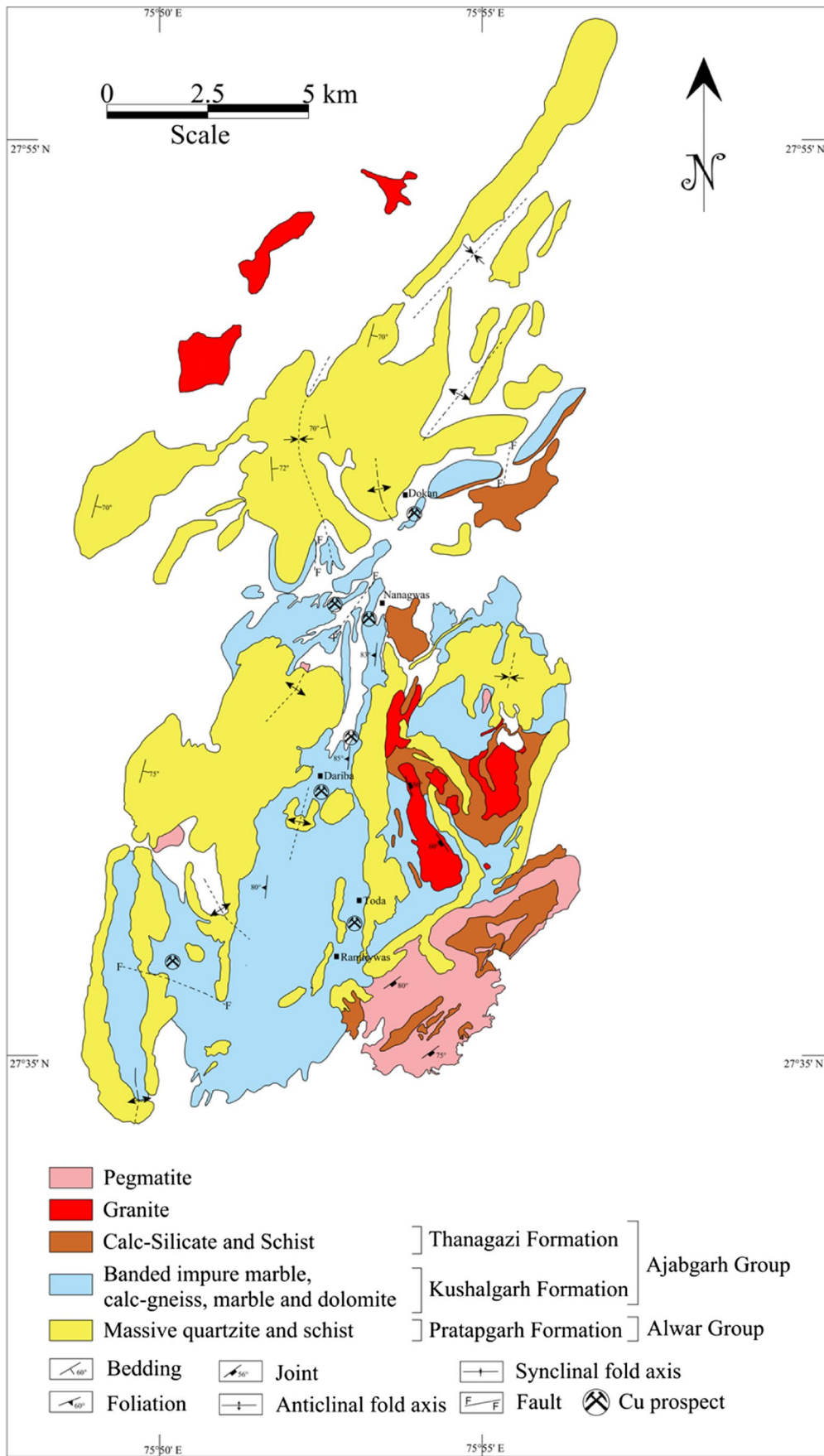
Legend:

- Pegmatite
- Granite
- Calc-Silicate and Schist — Thanagazi Formation — Ajabgarh Group
- Banded impure marble, calc-gneiss, marble and dolomite — Kushalgarh Formation
- Massive quartzite and schist — Pratapgarh Formation — Alwar Group

Bedding   Joint   Synclinal fold axis
Foliation   Anticlinal fold axis   Fault   Cu prospect

◄**Fig. 2** Geological map of the Nim Ka Thana Copper Belt showing location of the copper prospects (Data source: Geological Quadrangle Map, Geological Survey of India, 2013)

## Sampling and analytical method

### Sampling

Petrography, mineral chemistry, fluid inclusion, and sulfur isotope studies were carried out on samples from the three major prospects viz. Nanagwas, Dariba North, and Toda–Ramliyawas of the Nim Ka Thana Copper belt. Mainly drilled core samples of ore zones and host rocks were collected for the study. For Petrography and mineral chemical study, polished thin section and polished section were prepared from bed rock samples and drill core samples. Fluid inclusion samples also were collected from drill core of quartz veins associated with the copper mineralization. For sulfur isotopic compositions, pure fraction of sulfide minerals viz. chalcopyrite, bornite, chalcocite, pyrite, pyrrhotite, and galena were collected from different ore zones of these three prospects for sulfur isotopic composition.

### Analytical method

Thin polished sections of ore body and host rock were prepared to study the textural relationship and mineral chemistry of sulfide minerals and their associated gangue minerals. The mineral compositions of sulfide minerals of Cu-ore body were determined using CAMECA SX-100 electron microprobe at EPMA Laboratory, NCEGR, Geological Survey of India, Faridabad. The analytical condition for sulfide mineral was maintained through accelerating voltage of 20 kV and current 15 nA with peak counting times of 10 s for all elements. The beam size for the analysis was 1 μm. All the natural standards were used for calibration of the instrument. The fluid inclusions petrography was carried out under a high magnification microscope, and the temperatures of the thermally induced phase transitions in fluid inclusions were investigated using a calibrated LINKAM THMSG 600 heating/freezing stage at Fluid Inclusion Laboratory of NCEGR, Geological Survey of India, Bengaluru and Fluid Inclusion Laboratory of CPL, Geological Survey of India, Kolkata. The heating/freezing stage is fitted with the Olympus BX-50/Leica DM 2500 transmitted light microscope attached with the LNP-95-LTS liquid nitrogen cooling unit and temperature control with the digital video capturing system. The system was calibrated, and the reproducibility of measurements at room temperature was tested using natural fluid inclusion standards from quartz crystals tested in other established laboratories, as well as synthetic $H_2O$-$CO_2$ inclusions and Millipore $H_2O$ standards supplied by LINKAM. Estimated accuracy is $\pm 0.1$ °C at temperature below 30 °C

and $\pm 1.00$ °C at temperature above 30 °C. Reproducibility of the results of heating above 300 °C has been tested and found to be $\pm 2$ °C to 3 °C. The software used for the study of fluid inclusions is LINKSYS. The temperature was controlled with the LINKSYS software. Freezing and heating of the samples were carried out depending upon the inclusion type. Freezing experiments were performed first on all sections/wafers to avoid the decrepitation of inclusions followed by heating, following the procedure given by Roedder (1984). The data taken during heating include final melting temperature of ice ($Tf_{ice}$) to determine the salinity of aqueous phase. During the heating of the fluid inclusions, attempts were made to measure the total homogenization temperature ($Th_{Total}$). Initial melting of $CO_2$ phase ($Tm\ CO_2$), final melting of ice ($Tm\ ice$), final melting of clathrate ($T_{Clath}$), homogenization within $CO_2$ phase ($Th\ CO\ L–V$), and total homogenization of inclusion contents ($Th$) were measured. The apparatus operates in the temperature range of $-195$ to 600 °C to calculation of density and salinity of the inclusions.

Sulfur isotopic study was performed in IRMS Laboratory, NCEGR (PPOD), Geological Survey of India (GSI), Bengaluru and IRMS Laboratory, Birbal Sahni Institute of Paleoscience (BSIP), Lucknow, India. Pure fraction of sulfide minerals were separated using a binocular microscope and confirmed using XRD analysis. The separated powdered samples were analyzed for sulfur isotopes in continuous flow mode using Isotope Ratio Mass Spectrometer (Make: SerCon Geo 20–20 at GSI and Thermo Scientific MAT 253 at BSIP), using automated nitrogen and carbon analyzer for gas, solids, and liquid (ANCA-GSL) peripheral system. About 35–50 mg powder of each sulfide minerals, weighed into tin capsules, were packed manually and placed within the auto-sampler unit above the ANCA and the positions were marked. About 35–50 mg powder of each sulfide minerals, weighed into tin capsules, were packed manually and placed within the auto-sampler unit above the ANCA and the positions were marked. During analysis, each tin capsule was dropped one by one into a furnace at 1050 °C with an additional oxygen pulse. The tin ignites and burns exothermally in presence of oxygen and the temperature rises ~ 1800 °C, oxidizing the sample. Water is removed by a trap containing anhydrous magnesium perchlorate and using a nafion dryer. The carrier gas used is helium (99.999%). The gas stream passes into a gas chromatograph where sulfur is separated and injected into a mass spectrometer for the analysis of the sulfur isotopes. The total analysis time for each sample is 550 s. Analytical techniques and fractionation mechanisms are described in detail by De Groot (2009) and Hoefs (2009). The NBS 123 (sphalerite) reference material was analyzed along with the samples to monitor data quality. All data are

**Fig. 3** Field photographs of host rock of copper minaeralization of NKTCB. **a** Impure banded marble with foliation; **b** impure dolomitic marble showing amphibolization; **c** drill core showing carbonaceous phyllite with sulfide mineralization; **d** quartz clast within ferruginised breccia; **e** quartz vein cross cutting impure banded marble; **f** tight fold in banded impure marble; **g**, **h** profuse malachite staining within the host rock
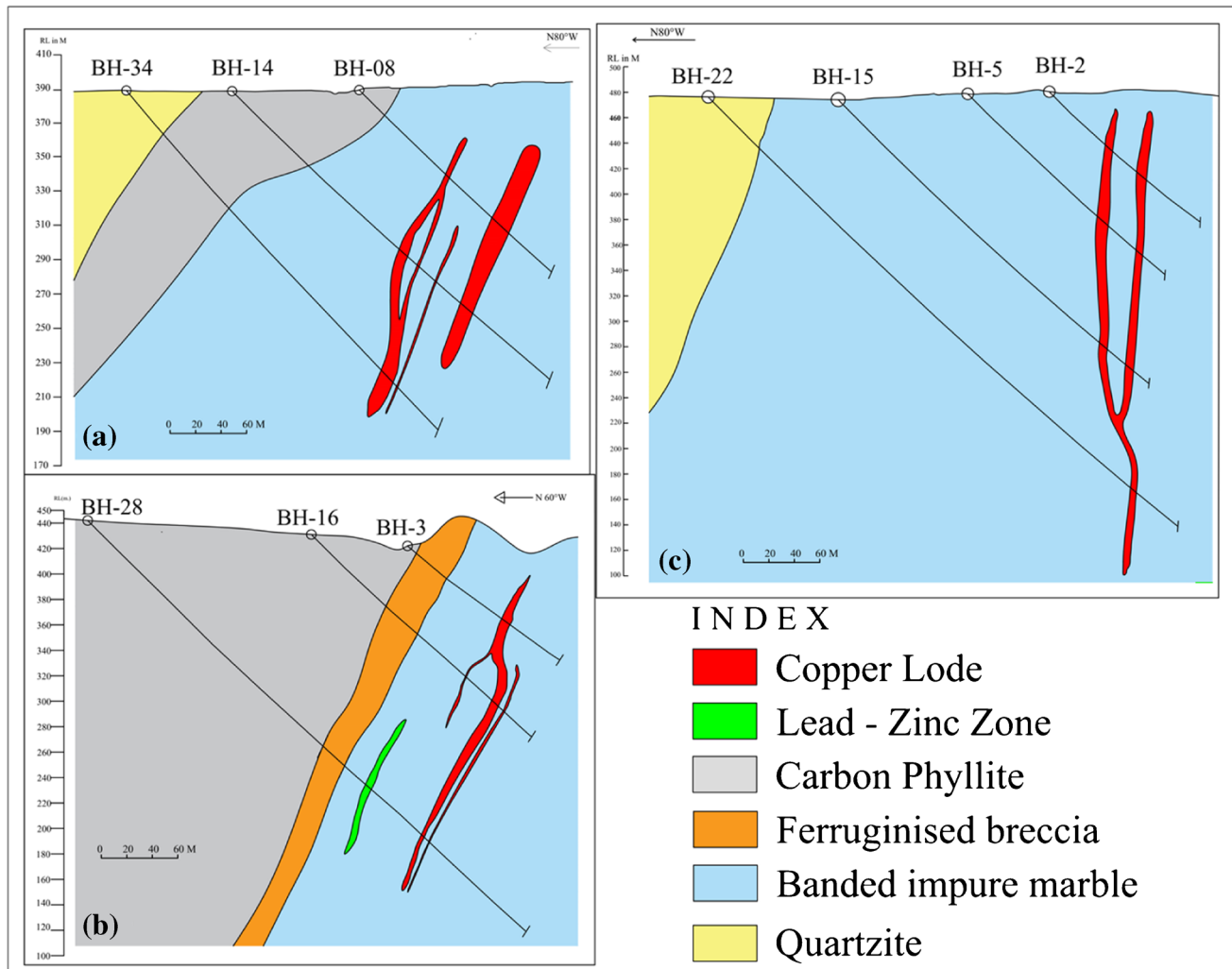
**Fig. 4** Geological cross section of different copper prospects shows disposition of copper ore body. **a** Nanagwas prospect, **b** Dariba North prospect, **c** Toda–Ramliyawas prospect

reported as delta per mil ($\delta^{34}$S ‰) relative to the Vienna Canyon Diablo Troilite (VCDT) (Zhang and Ding 1989). Repeated measurement of the NBS 123 sphalerite gives $\delta^{34}$S$_{VCDT}$(‰) of $17.44 \pm 0.23$‰, which is within the recommended value (Beaudoin and Taylor 1994).

## Results

### Petrography and mineral chemistry

#### Petrography of host rock

Host rock of the copper mineralization in NKTCB is banded impure marble. It exhibits alternate dark and light colored bands and ridge and furrow structure. The rock is mainly composed of calcite, biotite, quartz, and feldspar.

Garnet, hornblende, tremolite, actinolite, scapolite, staurolite, chlorite, and tourmaline are present as minor minerals (Fig. 6a–f). Magnetite, sphene, and specular hematite are present as accessory minerals. Orthoclase and plagioclase are also observed. The carbonate rich band (light colored) shows effect of recrystallization, where polygonal, subhedral grains of calcite forms triple point contact. The felsic bands (dark colored), composed of biotite, quartz, and albite also show granoblastic fabric defined by recrystallized grains of quartz and feldspar. A parallel arrangement of biotite flakes defines the foliation in impure marble (Fig. 6a, b). Swerving of foliation is observed around the garnet and hornblende grains (Fig. 6c, d). This indicates that these grains are syntectonic with the foliation plane and formed pressure shadow zone. Large elongated grains of tremolite and actinolite are also observed as clusters. Tremolite and actinolite are formed by the hydrothermal alteration. Two types of
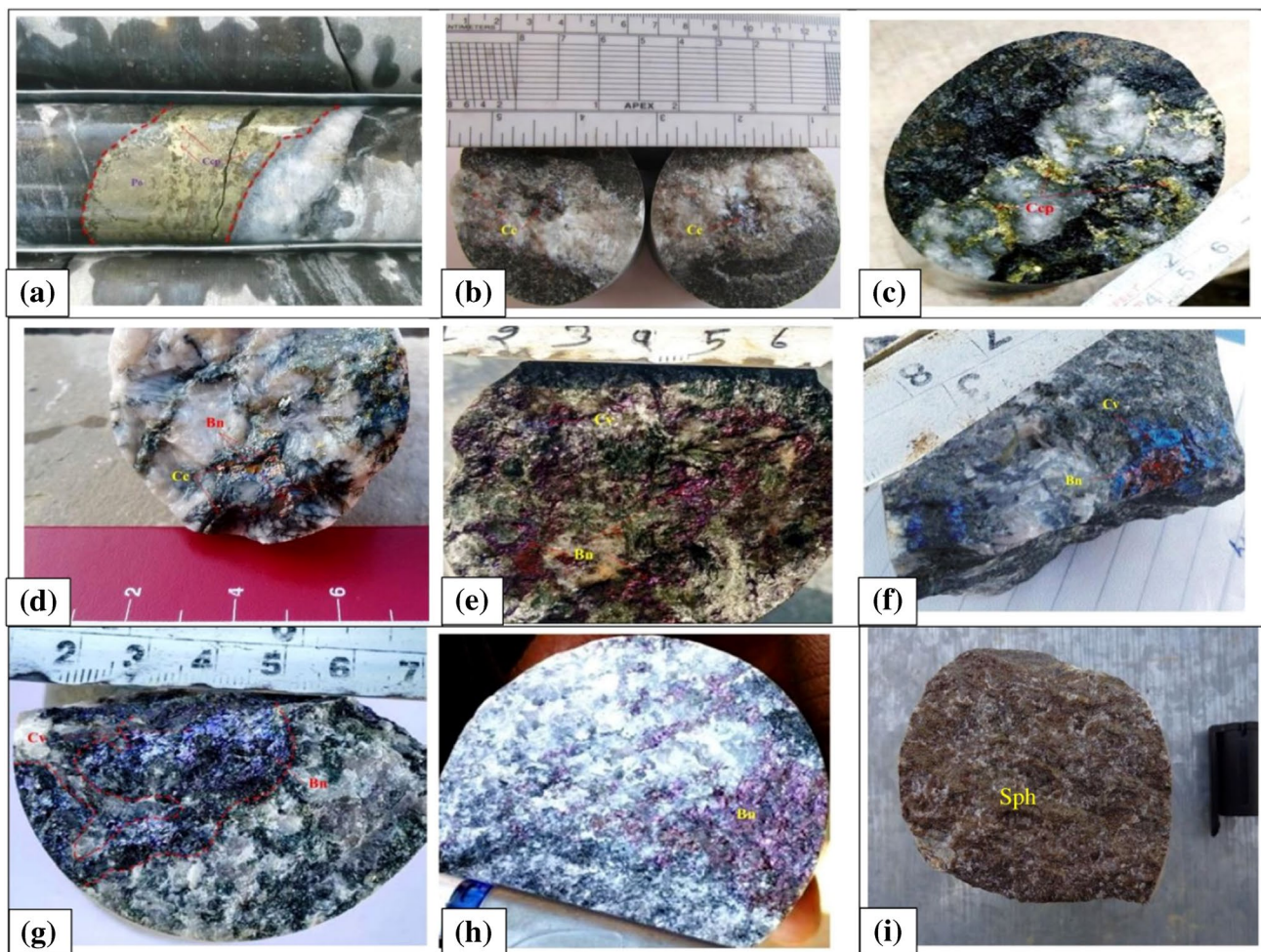
**Fig. 5** Photographs of drill cores showing copper mineralization in Nim Ka Thana Copper Belt. **a** Vein filled chalcopyrite with pyrrhotite and pyrite; **b** large chalcocite grain within quartz—calcite vein; **c** chalcopyrite associated with quartz vein; **d** bornite and chalcocite association within quartz vein; **e** bornite and covellite association within the amphibole rich zone in banded impure marble; **f** bonite and covellite association within quartz vein; **g** large bornite grain within quartz-calcite vein; **h** bornite within banded impure marble; **i** sphalerite and galena within banded impure dolomitic marble

scapolite are observed within the host rock; type-I is skeletal and associated with the ore minerals (Fig. 6e) and type-II is elongated and not associated with the ore minerals. Type-I scapolite was the product of alteration and type-II was the product of metamorphism. Tourmaline is also present within the host rock that indicates the boron metasomatism within the rock (Fig. 6f). It is also observed that the sulfide minerals were more within the biotite, amphibole, scapolite, and tourmaline rich zones. Sericitization and chloritization are also observed within the host rock.

## Petrography of ore minerals

Detailed ore petrography of Nim Ka Thana copper belt was carried out using drill core samples of ore zones. Both primary and secondary ore minerals are observed in the area.

Bornite, chalcocite, chalcopyrite, pyrite, pyrrhotite, galena, sphalerite, and covelite present as major ore minerals with decreasing order of abundance (Fig. 7a–l). Magnetite and specular hematite are also present with the Cu ore minerals. Digenite, mackinawite, native copper, pentlandite, Bi-phase, Ag-phase, and barite are present as minor ore minerals. Bornite, chalcocite, chalcopyrite, pyrite, pyrrhotite, galena, and sphalerite occur as primary ore minerals, whereas chalcocite, covellite, and digenite occur as secondary copper ore minerals. Primary ore minerals are showing straight and equilibrium grain boundary. Equilibrium grain boundaries are noted between chalcopyrite-bornite, bornite-pyrite, chalcopyrite-pyrite, and sphalerite-galena pairs. Straight and equilibrium grain boundaries of these mineral pairs indicate that these minerals were formed at the same time and from the same type of ore fluids. At places, bornite–chalcopyrite

**Fig. 6** Photomicrographs of banded impure marble showing **a** parallel arrangements of calcite and biotite defining foliation plane; **b** parallel arrangements of biotite flakes; **c** biotite flakes warping around amphibole grains; **d** garnet porphyroblast within host rock; **e** anhedral scapolite (Scp) grains within host rock, these scapolite are the product of hydrothermal alteration; **f** tourmaline grain within banded impure marble indicating boron metasomatism
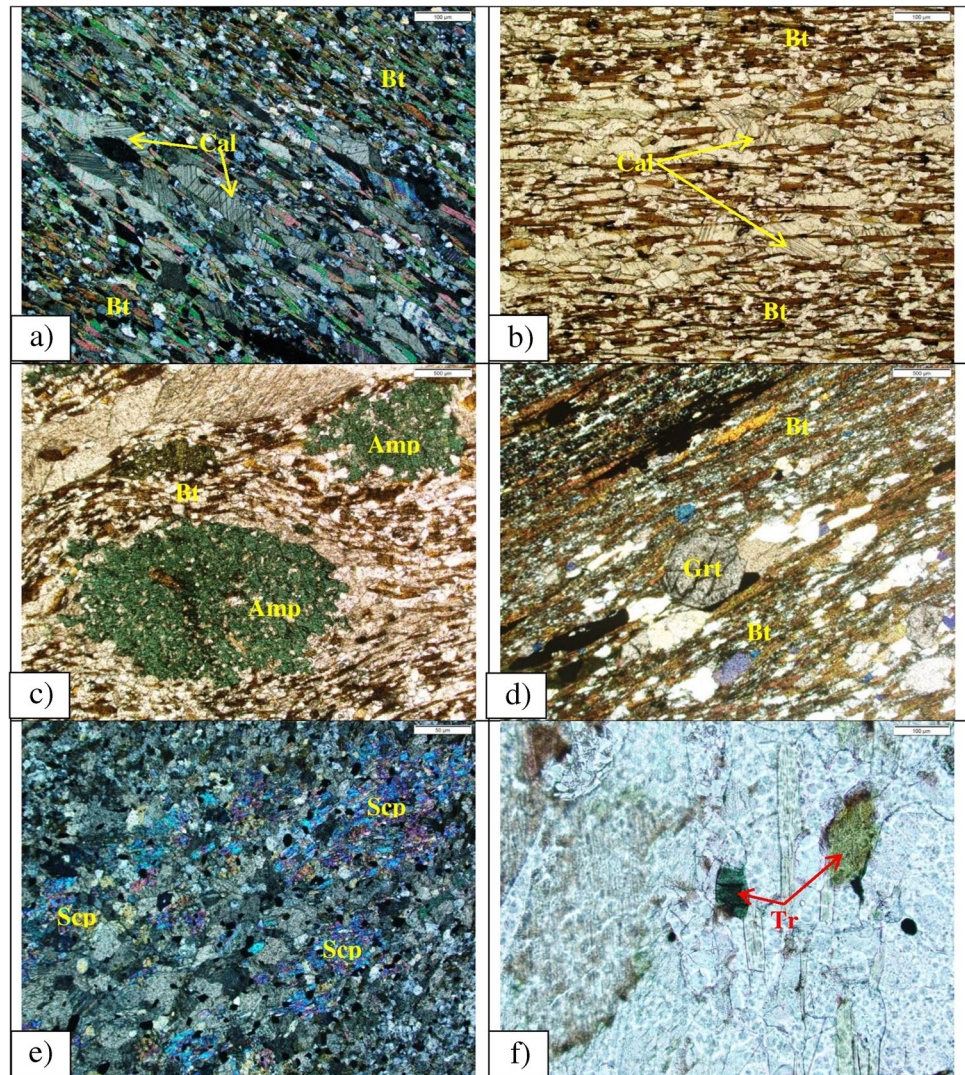


pair shows invaded and concave-convex grain boundary, indicating that these two minerals are in equilibrium state. Vermicular intergrowth between bornite and chalcocite is also observed (Fig. 7i). This type of intergrowth is quite possibly the result of simultaneous competitive growth of two phases. In the ore zone, replacement texture also observed between chalcopyrite–bornite, chalcopyrite–chalcocite, bornite–chalcocite, chalcocite–covellite, and bornite–digenite pairs where the former is replaced by the latter. Fine dusty dissemination of bornite and chalcocite is also observed within the host rock. At places, foliation parallel sulfide mineralization is also observed. Fracture filled bornite (Fig. 7c), chalcopyrite, and chalcocite are also observed within the host rock. Stringer of chalcopyrite within bornite grain is also observed and this indicates remobilization of ore. Layer parallel pyrite mineralization observed within the carbonaceous phyllite. These pyrites are mostly euhedral in shape. At places, framboidal pyrite also observed. These pyrites mostly formed during diagenetic process.

## Mineral paragenesis

In this belt, sulfide mineralization was formed at three different stages (Fig. 8). Stages of mineralization are identified by the assemblages of ore and gangue minerals, texture of ore minerals, and their grain boundary relationship. Major copper mineralization was formed during the second stage.

**Stage-1: sedimentary stage** The mineral assemblages in this stage are pyrite, pyrrhotite, magnetite, calcite, and quartz. In this stage, bedding parallel and $S_0//S_1$ pyrite mineralization is observed within the banded impure marble and carbonaceous phyllite rock unit. Pyrrhotite and euhedral magnetite are also associated with the pyrite mineralization. Different bands of pyrite and magnetite are observed.

**Stage-2: hydrothermal stage** In this stage, vein filling, fracture filling, stringers, patchy, and semi-massive type copper ores were formed. This second stage of mineralization is
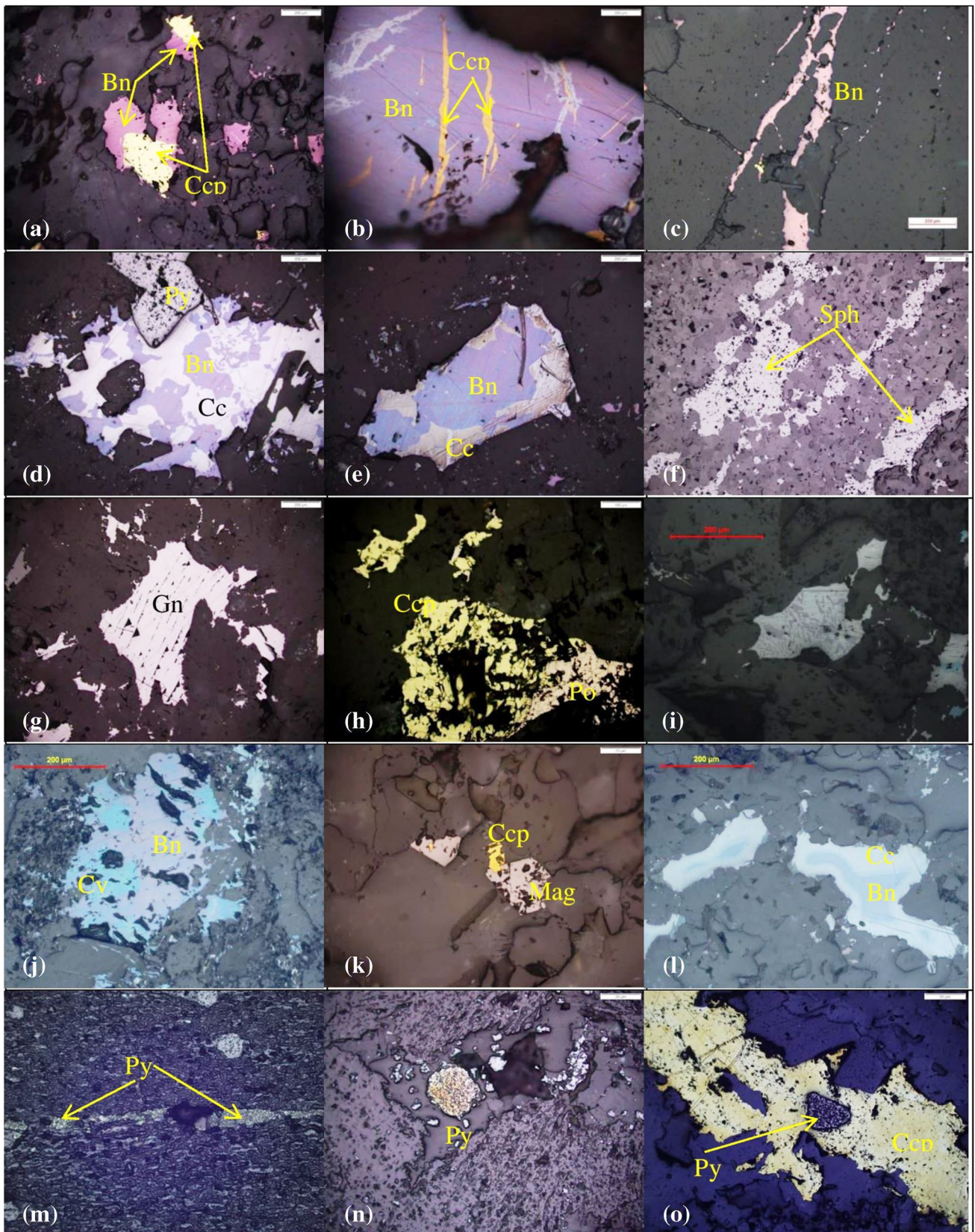
◀**Fig. 7** Photomicrographs showing different ore mineral assemblages with their alteration pattern and textural relationship. **a** Bornite and chalcopyrite sharing straight grain boundary indicating simultaneous crystallization; **b** blabes of chalcopyrite grains within bornite; **c** vein filled bornite within the host rock indicating crystallization of hydrothermal ore fluid along fracture plane; **d** chalcocite replacing early phase bornite which shares equilibrium grain boundary with pyrite; **e** Replacement texture between bornite and chalcocite where the former is replaced by the latter; **f)** Stringers of sphalerite within the host rock; **g)** Galena within the host rock; **h** chalcopyrite and pyrrhotite sharing mutual grain contact; **i** myrmekite intergrowth between bornite and chalcocite; **j** replacement texture between bornite and covellite, covellite replacing bornite; **k** mutual intergrowth in between chalcopyrite and magnetite; **l** replacement texture between bornite and chalcocite, chalcocite occurring as rim over bornite grain indicating supergene enrichment; **m** sedimentary pyrite within carbon phyllite, these pyrites are foliation parallel; **n** diagenetic euhedral shaped pyrite associated with magnetite within impure marble; **o** hydrothermal pyrite associated with chalcopyrite. (*Ccp* Chalcopyrite, *Bn* bornite, *Cc* chalcocite, *Py* pyrite, *Po* pyrrhotite, *Cv* covellite, *Gn* galena, *Sph* sphalerite, *Mag* magnetite)

only observed within the banded impure marble. Most of the hydrothermal alteration, i.e., amphibolization, chloritization, biotitization, sericitization, silicification, and ferruginised breccia, was formed during this stage. Bornite, chalcopyrite, and chalcocite are the major ore minerals in this stage. Pyrite, pyrrhotite, magnetite, specularite, sphalerite, galena, mackinawite, and pentlandite are also represented in the hydrothermal stage.

**Stage-3: replacement stage** This stage exhibits the replacement of early formed ore minerals. In this stage, bornite and chalcopyrite are replaced by chalcocite, covellite, and digenite. Replacement of chalcopyrite by bornite is also observed.

### Mineral chemistry of ore and gangue minerals

Mineral chemistry of major ore minerals and associated gangue minerals were determined using EPMA analysis. Chalcopyrite, bornite, chalcocite, covellite, pyrite, pyrrhotite, digenite, native-Cu, mackinawite, galena, sphalerite, and pentlandite were confirmed (Table 1). Sharma et al. (2015) also reported native silver, argentite, parkerite, corrollite, and wittichenite, in addition to the significant copper-bearing mineral phases. Trace element analysis of major Cu-bearing ores indicates that the tellurium (Te) content is much higher in chalcopyrite (up to 0.23 wt%) than that in bornite (up to 0.14 wt%) and chalcocite (up to 0.10 wt%). Bornite shows higher Ag concentration compared to other minerals. Ag concentration in bornite is up to 0.10 wt%, whereas it is up to 0.07 wt% in chalcocite and up to 0.06 wt% in chalcopyrite. Bi concentration is also observed in a few bornite grains up to 5.05 wt%. Co/Ni ratio was used to determine the environment of ore formation. Co/Ni ratio < 1

indicates sedimentary environment and > 1 indicates hydrothermal source (Bralia et al. 1979; Bajwah et al. 1987; Raymond 1996; Craig et al. 1998; Clark et al. 2004; Cook et al. 2009; Zhao et al. 2011). Co concentration in pyrite and pyrrhotite ranges from 0.04 to 1.66 wt% and 0.01–0.10 wt% respectively. Ni concentration in pyrite and pyrrhotite grain varies from 0.001 to 0.61 wt% and 0.001–0.35 wt%. Co/Ni ratio in pyrite and pyrrhotite varies from 0.20–20 and 0.19–15 respectively. In NKTCB, based on Co/Ni ratio, two types of pyrite and pyrrhotite were identified which are occurring in association with major copper ores. Type-I pyrite and pyrrhotite are sedimentary origin (Co/Ni ranges 0.20 to 0.70) and type-II pyrite and pyrrhotite are hydrothermal in origin (Co/Ni ranges 1.1 to 19). EPMA analysis of magnetite grains indicates that $TiO_2$ and $Al_2O_3$ content in magnetite grain vary from 0.05–7.92 wt% and 0.05–0.14 wt%. The hydrothermal magnetite is commonly depleted in Ti (< 2 wt%) and Al (< 1 wt%) (Ray and Webster 2007; Dupuis and Beaudoin 2011; Nadoll et al. 2012, 2014; Dare et al. 2012, 2014). Low $TiO_2$ and $Al_2O_3$ concentration indicates the presence of hydrothermal magnetite within the mineral system. Amphibole, biotite, feldspar (plagioclase and orthoclase), chlorite, garnet, scapolite, and tourmaline were also identified using EPMA. Mineral chemistry of amphiboles associated with ore zones is mostly calcic in nature and tschermakite-hornblende to ferro-tschermakite types. Biotite that associated with the ore zones are plogophite to annite variety. Chlorite grains were mostly ripidolite. Cl and F content in biotite vary from 0.06–1.27 wt% and 0.10–1.26 wt% respectively. Na enrichment is observed within the scapolite which is associated with mineralized zones. $Na_2O$ in scapolite associated with the ore zones varies from 6.0–7.9 wt%.

### Fluid inclusion study

Nim Ka Thana copper deposit is traversed by numerous quartz-calcite veins which are associated with the copper mineralization. Mineralized quartz veins were used for fluid inclusion petrographic and microthermometric studies in order to characterize the ore fluids. Fluid inclusion microthermometry has been abundantly used to define fluid composition, ore-forming processes, and pressure temperature conditions. Doubly polished section of quartz veins were mainly used for the petrography and microthermometry. Large numbers of doubly polished sections were prepared for proper microthermometry. Only large isolated primary inclusions were used for the microthermometry study. Caution was also taken to correctly identify primary and secondary fluid inclusions to ensure that the former were analyzed. A total number of 215 inclusions were used for microthermometry study (Table 2).

| Stage Mineral | Stage - I Sedimentary | Stage - II Hydrothermal | Stage - III Replacement |
|---|---|---|---|
| Pyrite | ▬▬▬▬ | ▬▬ | |
| Pyrrhotite | ▬▬▬ | ▬▬ | |
| Magnetite | ▬▬ | ▬▬ | |
| Specularite/ Hematite | | ▬▬ | ▬▬ |
| Chalcopyrite | | ▬▬▬▬▬ | |
| Bornite | | ▬▬▬ | ▬▬ |
| Chalcocite | | ▬▬ | ▬▬ |
| Sphalerite | | ▬▬▬ | |
| Galena | | ▬▬ | |
| Diagenite | | | ▬▬▬ |
| Covellite | | | ▬▬ |
| Mackinawite | | ▬▬▬ | |
| Pentalandite | | ▬▬▬ | |

**Fig. 8** Paragenetic sequence of NKTCB showing evolution of copper mineralization with respect to various oxide and sulfide minerals based on relationships between host rock mineral assemblages, ore textural, and microstructural relationships

## Fluid inclusion petrography

Fluid inclusion types were identified using detailed petrographic observation and fluid inclusion assemblage's methods in accordance with the classification principles and techniques outlined by Roedder (1984). To correlate different textural features of fluid inclusions with equilibration path using morphology of fluid inclusions, an attempt was made in the light of new experimental studies by Bodnar et al. (1989). Petrographic observations indicate that the fluid inclusions are widely distributed in quartz. The petrography of the fluid inclusions was conducted in accordance with the following rules: the isolated fluid inclusions and randomly distributed groups of fluid inclusions hosted in quartz crystals were interpreted as primary in origin, and those aligned along microfractures in the trans-granular trails were interpreted as secondary (Roedder 1984; Goldstein and Reynolds 1994; Van Den Kerkhof and Hein 2001). Primary inclusions are in various shapes, i.e., oval, spherical, rounded, irregular, and facetted. Secondary inclusions show rounded, sub-rounded, and faceted shape in a linear pattern. The study of quartz section indicates that liquid phases are more than the vapor phases. The ratio of occupied area in between vapor and liquid phases varies from 1:9 to 3:7. The size of the fluid inclusions varies from 1 to 69 μm. The size of vapor phase of water vapor/$CO_2$ bubbles varies from 0.50 to 6.85 μm. Based on the phases present, primary inclusions are grouped into three types: type-I aqueous bi-phase inclusions, type-II aqueous carbonic inclusions, and type-III carbonic monophase inclusions (Fig. 9).

**Type-I** Type-I inclusions are mainly aqueous type, bi-phase inclusions. They are isolated, irregular, rounded, and elliptical in shape. Sometimes, type-I inclusions show cluster nature, whereas secondary type-I inclusions are aligned along microfractures. These inclusions are more in number than the other type of inclusions and commonly they coexist with the type-II and III inclusions. These consist of $H_2O$ (l) and $H_2O$ (v) phases. The proportion of the vapor phase was typically about 10% to 15% by volume.

**Type-II** Fluid inclusions are aqueous carbonic type, bi-phase inclusions. These are characterized by the nucleation of vapor bubble on cooling and consist of $H_2O$ (l) and $CO_2$ (v) phases. They are irregular, elliptical, and faceted in shape. The proportion of the vapor phase is typically about 10% to 15% by volume.

**Type-III** Fluid inclusions are monophase carbonic inclusions and composed of pure carbonic fluid at room temperature containing $CO_2$ (v) or $CO_2$ (l). They are commonly dark in color with rounded, subrounded, and elliptical in shape. They mostly coexist with the type-I inclusions.

## Microthermometry

**Type-I** Fluid inclusion froze at temperatures mainly between − 63 and − 78 °C. During the heating runs, the first melting (eutectic) temperature (Teu) was observed, ranging from − 45 to − 20.2 °C with an average of − 31.3 °C. This suggests that the major component in aqueous phase is $NaCl \pm FeCl_2$ in the fluid system. The maximum eutectic temperature − 45 °C may indicate the presence of $FeCl_2 \pm MgCl_2$ with NaCl and $H_2O$ (Shepherd et al. 1985). The final melting temperature of ice (Tm, ice) ranges from − 0.4 to − 12.9 °C corresponding salinities of 0.33 wt.% to 16.80 wt.% NaCl eq. The range of homogenization temperature varies from 121.5 to 390.1 °C. The density of aqueous inclusions varies from 0.56 to 1.02 g/cm³ with an average of 0.87 g/cm³ (Fig. 10).

**Type-II** The initial ice melting eutectic temperatures (Te) range from − 26 to − 36.3 °C. This suggests that the major component in aqueous phase is $NaCl \pm MgCl_2$ in the fluid system. The final ice melting temperature varies from − 0.9 to − 4.7 °C which corresponds to salinity ranging from 1.48 to 7.39 wt% NaCl equivalents following the equations (Bodnar 1983; 1993). The melting temperature of solid $CO_2$ ranges from − 56.6 to − 62.1 °C. The homogenization temperature of $CO_2$ varies from − 5 to 24.5 °C. The density of aqueous carbonic phase varies from 0.64 to 0.98 g/cm³. The homogenization temperature (Th$_{total}$) varies from 110 to 375 °C.

**Table 1** Mineral Chemistry of sulfide minerals of Nim Ka Thana Copper Belt (values in wt%)

| Minerals | Fe | Cu | Zn | Ni | Co | As | S | Ag | Cd | In | Sn | Ba | Te | Au | Pb | Total |
|---|---|---|---|---|---|---|---|---|---|---|---|---|---|---|---|---|
| Pyrite | 46.68 | 0.09 | 0 | 0.1 | 0.04 | 0.02 | 52.89 | 0 | 0 | 0 | 0 | 0.03 | 0.05 | 0 | 0 | 99.9 |
| Pyrite | 46.31 | 0.52 | 0 | 0.17 | 0.12 | 0.09 | 52.27 | 0.02 | 0.05 | 0 | 0 | 0 | 0 | 0 | 0 | 99.55 |
| Pyrite | 46.23 | 0 | 0 | 0.26 | 0.04 | 0.06 | 52.77 | 0 | 0.01 | 0.01 | 0.1 | 0 | 0.02 | 0 | 0 | 99.5 |
| Pyrite | 46.38 | 0.01 | 0.01 | 0.07 | 0.24 | 0 | 53.23 | 0.02 | 0 | 0.04 | 0 | 0 | 0.13 | 0 | 0 | 100.13 |
| Pyrite | 46.21 | 0.03 | 0 | 0.06 | 0.24 | 0.05 | 53.34 | 0 | 0 | 0.17 | 0 | 0 | 0 | 0.02 | 0 | 100.12 |
| Pyrite | 45.24 | 0 | 0 | 0.14 | 0.23 | 0.05 | 49.62 | 0 | 0.07 | 0.12 | 0.04 | 0 | 0 | 0 | 0 | 95.51 |
| Pyrrhotite | 60.44 | 0.03 | 0.02 | 0.08 | 0.04 | 0.05 | 38.51 | 0.03 | 0.05 | 0 | 0.08 | 0 | 0 | 0.02 | 0 | 99.35 |
| Pyrrhotite | 62.08 | 0 | 0 | 0.1 | 0.04 | 0.14 | 36.13 | 0.02 | 0.02 | 0 | 0 | 0 | 0 | 0 | 0 | 98.53 |
| Pyrrhotite | 62.6 | 0.05 | 0 | 0.03 | 0.06 | 0.08 | 35.19 | 0 | 0 | 0 | 0 | 0 | 0 | 0 | 0 | 98.01 |
| Pyrrhotite | 61.11 | 0 | 0 | 0.03 | 0.05 | 0.02 | 36.8 | 0.02 | 0.02 | 0.05 | 0 | 0 | 0.03 | 0.11 | 0 | 98.24 |
| Chalcopyrite | 29.69 | 34.32 | 0 | 0 | 0 | 0.03 | 35.16 | 0.03 | 0 | 0.04 | 0 | 0.01 | 0 | 0.07 | 0 | 99.35 |
| Chalcopyrite | 29.74 | 33.54 | 0.07 | 0 | 0.02 | 0.05 | 35.87 | 0 | 0 | 0.01 | 0 | 0.02 | 0.1 | 0 | 0 | 99.42 |
| Bornite | 11 | 62.69 | 0.06 | 0 | 0.03 | 0.05 | 25.41 | 0.06 | 0 | 0.01 | 0 | 0.11 | 0 | 0.02 | 0 | 99.44 |
| Bornite | 10.62 | 62.61 | 0.03 | 0 | 0 | 0.05 | 25.93 | 0 | 0.03 | 0 | 0 | 0.21 | 0 | 0 | 0 | 99.48 |
| Chalcocite | 0.17 | 78.87 | 0.03 | 0.02 | 0 | 0.11 | 20.31 | 0.02 | 0.05 | 0 | 0.11 | 0.16 | 0 | 0.11 | 0 | 99.96 |
| Chalcocite | 0.17 | 78.87 | 0.03 | 0.03 | 0 | 0.11 | 20.31 | 0.02 | 0.05 | 0 | 0.11 | 0.16 | 0 | 0.11 | 0 | 99.97 |
| Chalcocite | 0.14 | 78.55 | 0 | 0 | 0 | 0.06 | 19.86 | 0.04 | 0 | 0.06 | 0.11 | 0.2 | 0.1 | 0 | 0 | 99.12 |
| Chalcocite | 0 | 79.02 | 0.06 | 0 | 0 | 0 | 20.84 | 0.01 | 0.01 | 0 | 0 | 0.14 | 0 | 0.05 | 0 | 100.13 |
| Galena | 1.35 | 1.8 | 0.17 | 0.01 | 0 | 0 | 13.37 | 0 | 0 | 0.15 | 0 | 0 | 0 | 0 | 82.17 | 99.02 |
| Galena | 1.64 | 2.2 | 0 | 0 | 0 | 0 | 12.99 | 0 | 0 | 0 | 0 | 0 | 0.04 | 0 | 82.67 | 99.54 |
| Sphalerite | 7.42 | 0 | 58.13 | 0 | 0.09 | 0.06 | 33.11 | 0.02 | 0.21 | 0.05 | 0 | 0 | 0 | 0.05 | 0 | 99.14 |
| Sphalerite | 7.6 | 0.39 | 58.62 | 0 | 0.06 | 0 | 33.12 | 0 | 0 | 0 | 0 | 0 | 0 | 0.08 | 0 | 99.87 |
| Mackinawite | 56.32 | 0.1 | 0.07 | 6.5 | 0.04 | 0 | 35.37 | 0.01 | 0.03 | 0.12 | 0 | 0.06 | 0 | 0.06 | 0 | 98.68 |
| Mackinawite | 55.9 | 0.18 | 0.01 | 6.22 | 0.07 | 0.05 | 35.35 | 0 | 0 | 0.09 | 0 | 0 | 0 | 0 | 0 | 97.87 |
| Pentlandite | 32.67 | 0.05 | 0 | 22.29 | 9.13 | 0.01 | 32.81 | 0.02 | 0.06 | 0 | 0 | 0 | 0 | 0 | 0 | 97.04 |
| Pentlandite | 41.11 | 0.02 | 0 | 14.84 | 5.69 | 0 | 34.97 | 0 | 0 | 0 | 0 | 0 | 0 | 0.03 | 0 | 96.66 |
| Barite | 2.67 | 0 | 0 | 0 | 0.01 | 0 | 10.22 | 0.01 | 0 | 0 | 0.02 | 52.51 | 0.03 | 0 | 0 | 65.47 |
| Barite | 2.95 | 0.02 | 0 | 0 | 0 | 0.03 | 9.5 | 0 | 0 | 0 | 0 | 51.66 | 0.07 | 0 | 0 | 64.23 |

**Type-III** Fluid inclusions show melting temperature (TmCO$_2$) varying from $-57.1$ to $-65.8$ °C and the maximum depression in TmCO$_2$ ($-60.2$ °C) indicates an admixture of other gases, most probably that of CH$_4$/N$_2$ (Brown and Lamb 1989; van den Kerkhof 1988). The temperature of homogenization of CO$_2$ into vapor phase ranges from $-23$ to 24.5 °C and density varies from 0.71 to 1.05 g/cm$^3$.

## Sulfur isotopes

A total of 46 samples were analyzed for sulfur isotopic composition of sulfide phases (chalcopyrite, pyrite, pyrrhotite, bornite, and chalcocite). Forty-four samples were collected from banded impure marble and two samples were collected from carbonaceous phyllite. The $\delta^{34}S_{VCDT}$ (‰) values show a wide range from $-37.85$ to $+6.33$‰ with mean value of $-3.06$‰ and standard deviation of 8.71‰ (Table 3). The $\delta^{34}S_{VCDT}$ (‰) values in pyrite ($n=18$) sample ranges from $-37.85$ to $+5.28$‰, chalcopyrite ($n=16$) sample ranges from $-10.42$ to $+5.92$‰ with an average of $-1.40$‰, bornite ($n=6$) sample ranges from $-10.32$ to $-2.90$‰ with an average of $-8.26$‰, chalcocite ($n=3$) sample ranges from 0.51 to $+6.33$‰ with an average of $-3.02$‰, pyrrhotite ($n=2$) sample ranges from 3.05 to 4.55‰, and galena ($n=1$) sample shows $-1.88$‰ (Fig. 11). Pyrite ($n=16$) from banded impure marble show $\delta^{34}S_{VCDT}$ (‰) values ranges from $-12.16$ to $+5.28$‰ with an average of $-0.40$‰, whereas pyrite from carbonaceous phyllite ($n=2$) show $\delta^{34}S_{VCDT}$ (‰) values from $-37.85$‰ to $-32.63$‰. Bornite, chalcopyrite, and chalcocite are the major ore minerals of the copper mineralized zones in the Nim Ka Thana Belt. Higher isotopic values were observed in chalcocite than bornite and chalcopyrite.

**Table 2** Fluid inclusion analysis data of Nim Ka Thana Copper Belt

| Descriptions | Type | Origin | TmCO$_2$ | Te | Tmice | ThCO$_2$ | Th total | Salinity (Wt% NaCl) | Density (gm/cc) |
|---|---|---|---|---|---|---|---|---|---|
| Aquaous inclusion | I | Primary | | $-20.2$ to $-45$ | $-0.4$ to $-12.9$ | | 121.5 to 391 | 0.33 to 16.80 | 0.56 to 1.02 |
| Aqueous carbonic inclusions | II | Primary | $-56.6$ to $-62.1$ | $-26$ to $-36.3$ | $-0.9$ to $-4.7$ | $-5$ to 24.5 | 110 to 375 | 1.48 to 7.39 | 0.64 to 0.98 |
| Carbonic Inclusion | III | Primary | $-57.1$ to $-65.8$ | | | $-23$ to 24.5 | | | 0.71 to 1.05 |

## Discussions

### Characteristics and evolution of ore forming fluids

At Nim ka thana copper belt, aqueous inclusions, aqueous carbonic, and carbonic inclusions are observed in the quartz-calcite veins. These inclusions show gradual changes in terms of distribution, homogenization temperature and salinity which provide important information on the nature and evolution of the ore forming fluids.

The characteristics of the quartz vein hosted fluid inclusions analyzed during the study are listed in Table 2. These inclusions have Tm values ranging from $-0.4$ to $-12.9$ °C, yielding calculated salinity of 0.33 to 16.80 wt% NaCl equivalent. They have density values in the range of 0.56 to 1.05 g/cc. Th values vary from 110 to 391 °C. The diagram of homogenization temperature versus salinity (Wilkinson 2001) of these data indicates that copper mineralization in the NKTCB records the isothermal mixing and the simple cooling of ore forming fluids with boiling by consideration of $H_2O$–$CO_2$–$NaCl$ phase diagram (Gehrig et al. 1979). The boiling of the ore-forming fluid is characterized by low salinity $CO_2$-rich fluid (Fig. 12).

In NKTCB, type-I inclusions are mainly liquid rich ($H_2O + NaCl$) and highly saline (0.33 to 16.80 wt% NaCl eqiv.), whereas type-II inclusions are mainly vapor rich with low salinity (1.48 to 7.39 wt% NaCl eqiv.). It was observed



**Fig. 9** Different types of fluid inclusions observed within mineralized quartz veins of NKTCB. **a** Primary bi-phase aqueous inclusions; **b** primary aqueous carbonic inclusions; **c** primary mono phase carbonic inclusions; **d** trails of secondary aqueous inclusions (S)
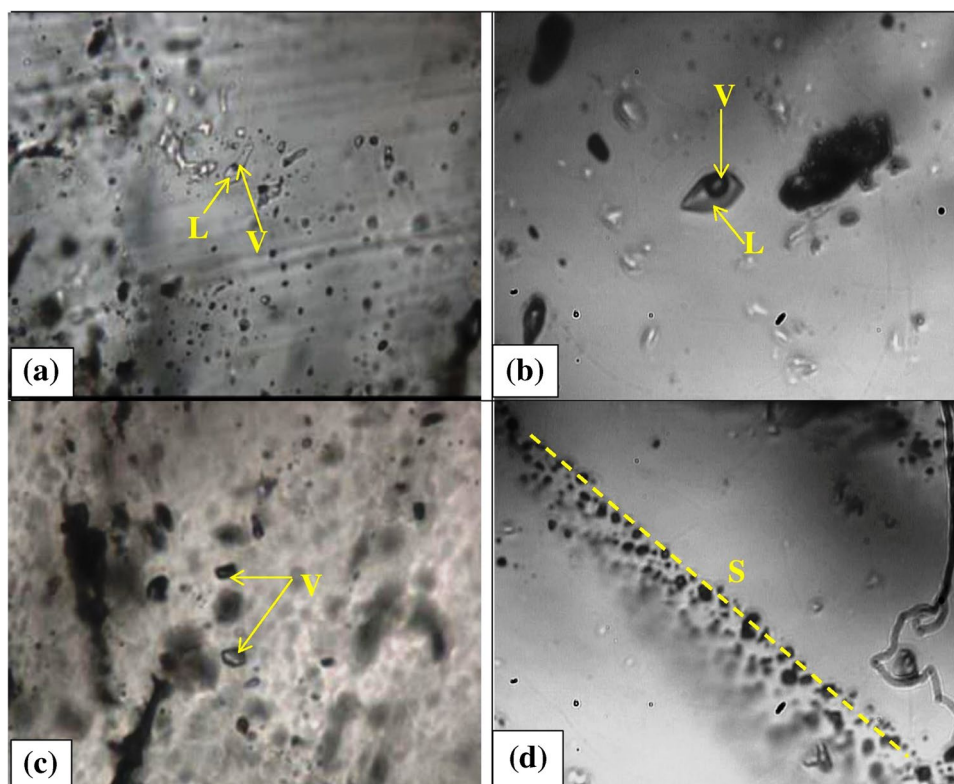
**Fig. 10** Histograms of **a** homogenization temperature, **b** salinity, and **c** density of fluid inclusion of quartz vein from Nim Ka Thana Copper Belt
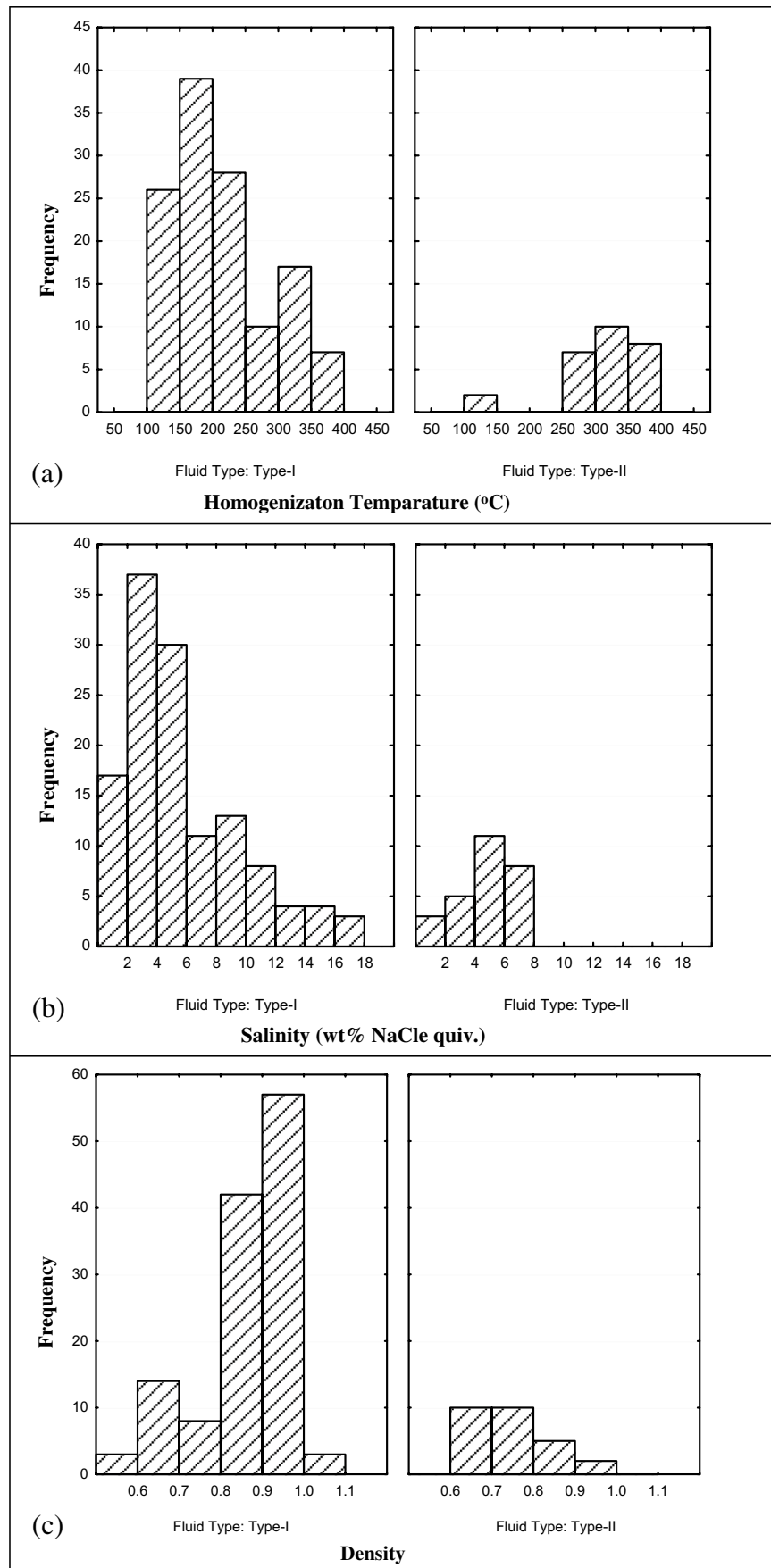
**Table 3** Sulfur isotope data of Nim Ka Thana Copper Belt

| Sl. No | Sample No | $\delta^{34}S_{VCDT}‰$ | Minerals | Prospect name |
|---|---|---|---|---|
| 1 | WNBH-8/S-1 | −7.29 | Chalcopyrite | Nanagwas Prospect |
| 2 | WNBH-8/S-2 | −6.47 | Bornite | |
| 3 | WNBH-12/S-1 | 1.88 | Pyrite | |
| 4 | WNBH-12/S-2 | 4.86 | Pyrite | |
| 5 | WNBH-13/S-1 | −7.88 | Bornite | |
| 6 | WNBH-15/S-2 | −0.29 | Chalcopyrite | |
| 7 | WNBH-16/S-1 | 0.35 | Chalcopyrite | |
| 8 | WNBH-18/S-2 | −6.02 | Bornite | |
| 9 | WNBH-18/S-3 | −2.33 | Pyrite | |
| 10 | WNBH-20/S-1 | −4.53 | Chalcopyrite | |
| 11 | WNBH-20/S-1A | −4.48 | Chalcopyrite | |
| 12 | WNBH-20/S-2 | −5.27 | Pyrite | |
| 13 | WNBH-20/S-3 | −0.47 | Pyrite | |
| 14 | WNBH-22/S-3 | −2.9 | Bornite | |
| 15 | WNBH-24/S-1 | 1.69 | Pyrite | |
| 16 | WNBH-25/S-4 | −2.71 | Chalcopyrite | |
| 17 | WNBH-27/S-3 | 1.26 | Pyrite | |
| 18 | WNBH-28/S-1 | −2.6 | Pyrite | |
| 19 | WNBH-29/S-1 | −0.21 | Chalcopyrite | |
| 20 | NW-1 | 5.92 | Chalcopyrite | |
| 21 | NW-2 | 2.2 | Chalcopyrite | |
| 22 | WNBH-20/S- 3A | −1.16 | Pyrite | |
| 23 | DNSI-2 | −32.63 | Pyrite | Dariba North Prospect |
| 24 | DNSI-3 | −37.85 | Pyrite | |
| 25 | DNSI-4 | 0.89 | Pyrite | |
| 26 | DNSI-5 | 1.39 | Pyrite | |
| 27 | DNSI-15 | 1.48 | Pyrite | |
| 28 | DNSI-17 | -5.47 | Pyrite | |
| 29 | DNSI-6 | 6.33 | Chalcocite | |
| 30 | DNSI-10 | 2.22 | Chalcocite | |
| 31 | DNSI-12 | 0.51 | Chalcocite | |
| 32 | DNSI-11 | 2.39 | Chalcopyrite | |
| 33 | DNSI-14 | 3.25 | Chalcopyrite | |
| 34 | DNSI-16 | −1 | Chalcopyrite | |
| 35 | DNSI-23 | 2.57 | Chalcopyrite | |
| 36 | DNSI-13 | −1.88 | Galena | |
| 37 | DNSI-8 | 4.55 | Pyrrhotite | |
| 38 | DNSI-9 | 3.05 | Pyrrhotite | |
| 39 | SDN-1 | 5.28 | Pyrite | |
| 40 | SDN-2 | 4.18 | Pyrite | |
| 41 | SDN-3 | 1.34 | Chalcopyrite | |
| 42 | RTRH-6/S-1 | −10.02 | Bornite | Toda Ramliyawas Prospect |
| 43 | RTRH -6/S-2 | −10.42 | Chalcopyrite | |
| 44 | RTRH-9/S-1 | −16.32 | Bornite | |
| 45 | RTRH-16/S-1 | −9.54 | Chalcopyrite | |
| 46 | RTRH-21/S-1 | −12.16 | Pyrite | |

that coexisting liquid-rich highly saline and vapor-rich low saline fluids in most hydrothermal deposits indicate the different fluid phases generated by immiscibility (Pichavant et al. 1982; Roedder 1992; Zhu et al. 2019). Type-I and type-II fluid inclusion in the study area indicate the presence of immiscibility of ore fluids.
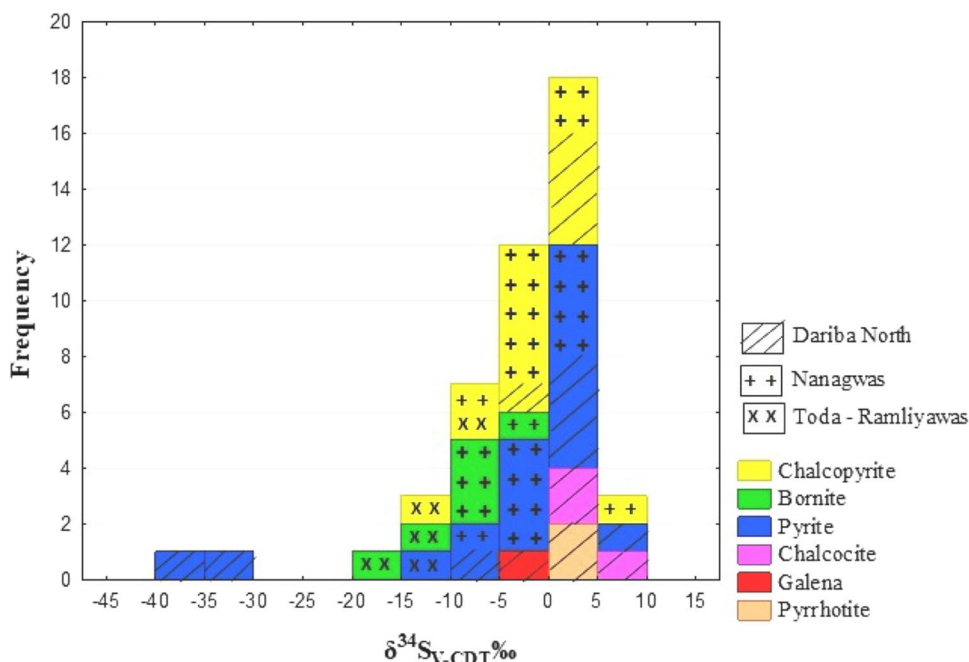
In metamorphic hydrothermal system, it is observed that fluids consist of mixture of $H_2O$ and $CO_2$, which are the most common fluid that release during the metamorphic reaction. The fluid inclusions in these deposits homogenize at temperature 250–400 °C and have wide range of $CO_2$ content. Salinity versus homogenization temperature diagram (after Kesler 2005) indicates that the ore fluids may be derived from the metamorphic fluids (Fig. 13). The higher values of salinity in ore fluids may be due to the connate brine which was preserved in original sediments and released during the metamorphism.

## Source of metals and ore forming fluids

The sulfur isotopic composition of sulfide minerals and ore forming fluids provide constraints on possible geological source of sulfur and other ore elements and help to decipher the condition of sulfide formation in ore deposits (Ohomoto 1972; Ohomoto and Rey 1979; Rollinson 1993; Ohomoto and Goldhaber 1997; Seal 2006; Hoefs 2009). In the current study of sulfur isotopes in NKTCB, $\delta^{34}S_{VCDT}$ (‰) values show a wide range from $-37.85$ to $+6.33$‰ in 46 sulfide samples. The isotopic data show bimodal distribution and they can be classified into two classes. Class-I shows $\delta^{34}S_{VCDT}$ (‰) values ranging from $-16.32$ to $+6.33$‰ and class-II shows value ranging from $-37.85$ to $-32.63$‰. Class-II values were obtained from pyrite samples within the carbonaceous phyllite unit which was devoid of copper ore minerals. Class-I values were obtained from pyrite, chalcopyrite, bornite, chalcocite, and galena samples within the banded impure marble unit which is the major host of copper mineralization.

The sulfur isotopic data of pyrite samples in carbonaceous phyllite shows negative $\delta^{34}S$ values indicating the presence of sedimentary source of sulfur by biogenic sulfate reduction. The predominantly low $\delta^{34}S$ values indicate bacterial sulfate reduction, whereas the higher values reflect formation of sulfides at much greater depth by thermochemical sulfate reduction (Riciputi et al. 1996). This negative $\delta^{34}S$ values can be due to the biological process or sudden changes in oxygen fugacity (Ohomoto 1972). In general, $\delta^{34}S$ value of sulfides in an euxinic environment ranges from $-20$ to $-40$‰ (Ohomoto and Rey 1979). The $\delta^{34}S$ value of pyrite from carbonaceous phyllite in NKTCB designates presence of a euxinic environment for sulfur source.

The $\delta^{34}S$ values of sulfide samples from banded impure marble show wide range of $\delta^{34}S$ values. $\delta^{34}S$ values range from $+6.33$‰ to $-16.33$‰ with an average value of $-1.45$‰. This wide range of sulfur isotope data indicates that sulfur has come from hydrothermally evolved source. It was observed that 15 samples of NKTCB fall into the range of magmatic sulfur source ($+2$‰ to $-2$‰). Consistent positive $\delta^{34}S$ values suggest that hydrothermal reduction of sulfate either dissolved in circulating sea water or dissolved from sulfate minerals might have been important for the production of isotopically heavy sulfides. During the mineralization, the oxygen fugacity at the depositional site might be presumably low and that reduced sulfate species to sulfide promoting the precipitation of copper sulfides (Druppel et al. 2006). Lighter isotopic values can be explained by the fractionation between $H_2S$ and oxidized S ($SO_2$, $SO_4$) in magmatic hydrothermal fluids that were initially oxidized.

**Fig. 12** Homogenization temperature vs. salinity diagram of fluid inclusions from study area (after Wilkinson (2001)). **a** Schematic diagram showing typical trends in homogenization temperature—salinity space due to various fluid evolution processes; **b** Homogenization temperature–salinity diagram illustrating typical ranges for inclusions from different deposit types including NKTCB (blue = Nangwas prospect; green = Dariba North prospect; red = Toda Ramliyawas prospect)
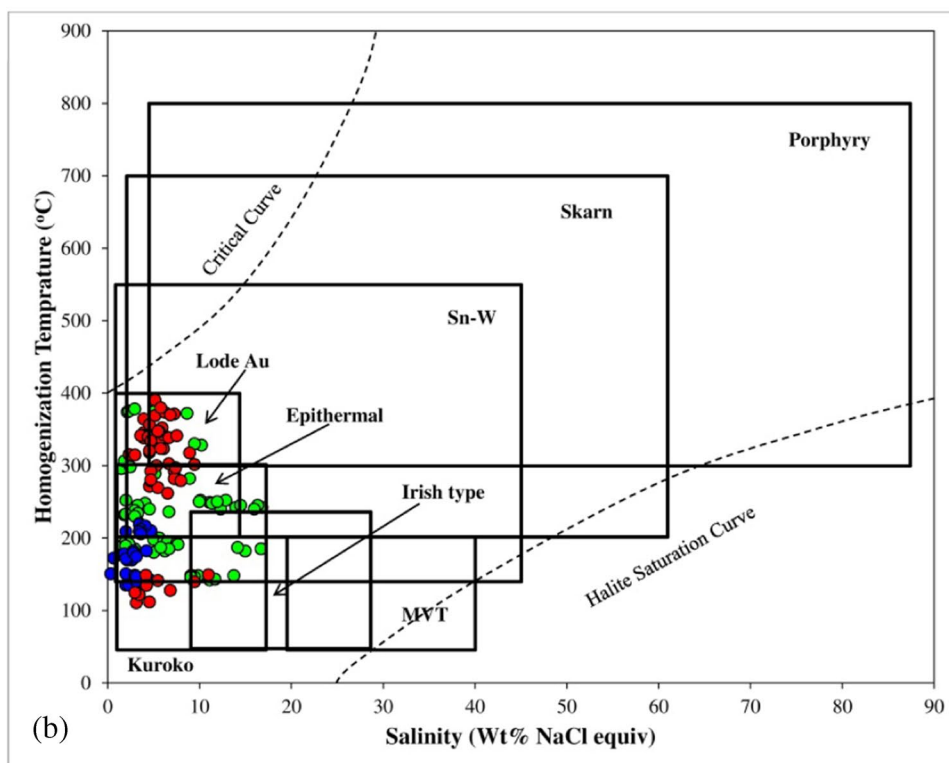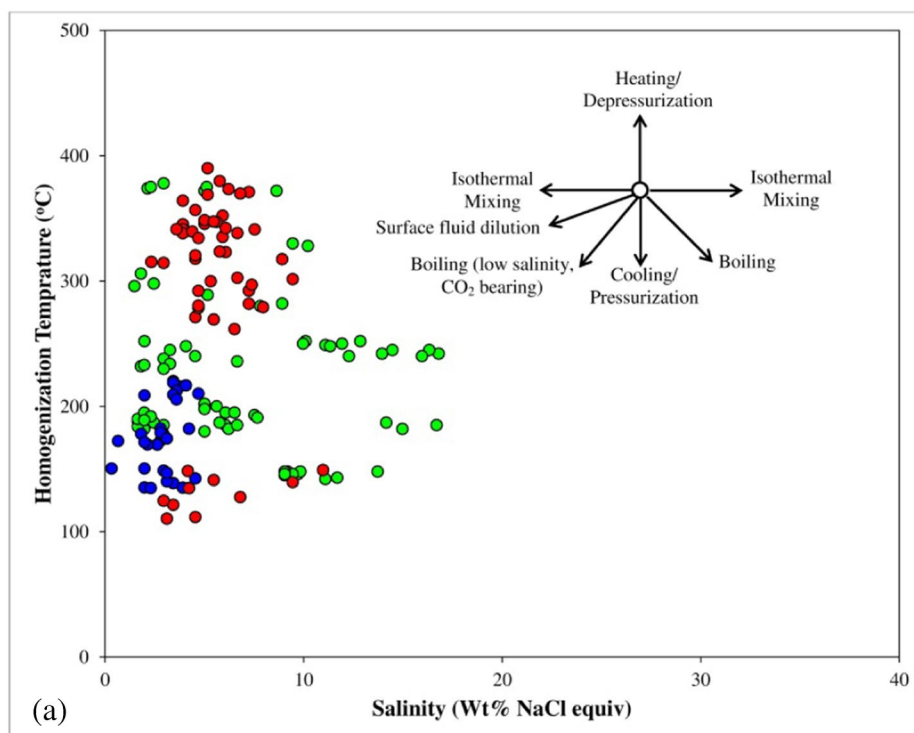


In NKTCB, the sulfur isotopic values of sulfides from banded impure marble and carbonaceous phyllite indicate two different sources of sulfur that involved in precipitation of sulfide minerals to form the copper mineralization. Preliminary sulfide mineralization was in the form of precipitation of pyrite in euxinic condition. This condition was supported by the presence of lighter isotopic values in pyrite samples of carbonaceous phyllite. Major copper mineralization was formed by the precipitation of copper sulfides from reduced oxidized hydrothermal fluids. This hydrothermal fluid was a mixture of magmatic and non-magmatic fluids. Fluid inclusion data supports higher salinity in ore fluids

**Fig. 13** Salinity versus homogenization temperature diagram of fluid inclusions from Nim Ka Thana Copper Belt after Kesler (2005) (blue = Nangwas prospect; green = Dariba North prospect; red = Toda Ramliya-was prospect)
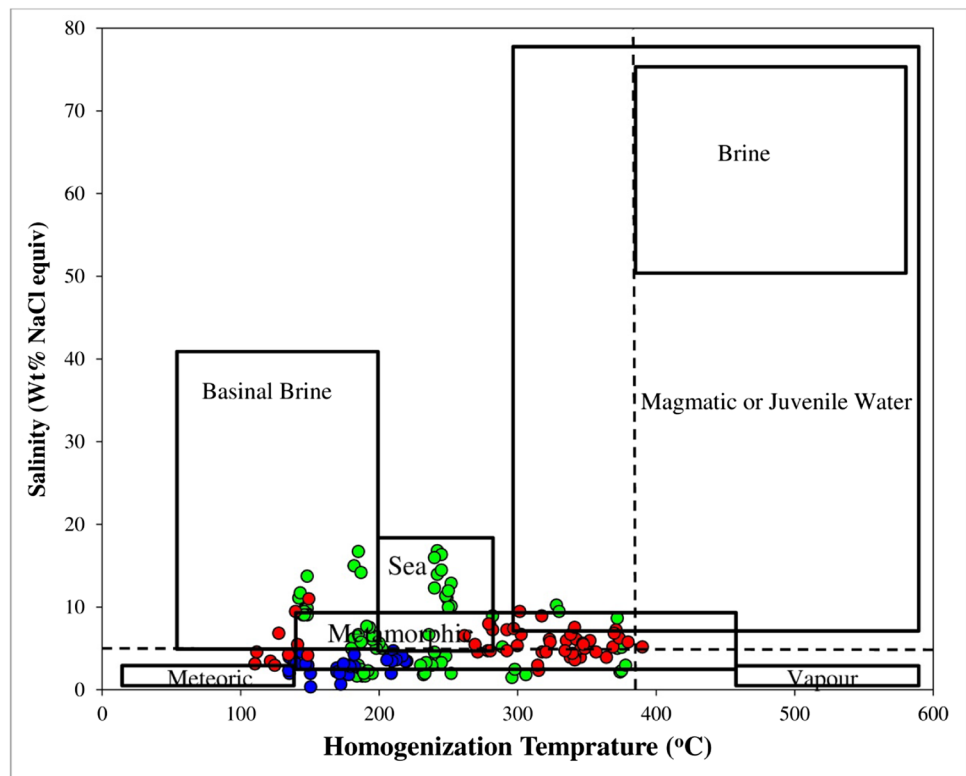


indicating a non-magmatic fluid. So it can be deciphered that ore-forming metals and sulfur come from a mixed source that is encompasses sedimentary and hydrothermal sources. The sulfur isotopic compositions of sulfide minerals are compared with the major geological sulfur reservoir and different types of copper deposit worldwide (Fig. 14).

## Genesis of ore mineral

Field observation, petrographic study, ore mineral chemistry, and sulfur isotope systematics indicate the superimposition of two genetic modes of sulfide mineralization in Nim Ka Thana Copper belt. First mode is denoted by syngenetic sedimentary type sulfide deposition and the second mode is of epigenetic hydrothermal type.

Syngenetic sedimentary mode is defined by the presence of bedding parallel, fine dusty dissemination of pyrite, pyrrhotite, and magnetite mineralization within carbonaceous phyllite and banded impure marble. Layer parallel euhedral and framboidal pyrite within carbonaceous phyllite indicate the sedimentary origin. These pyrites are diagenetic in origin. The sulfur isotopic values of pyrite from carbonaceous phyllite indicate an euxinic environment and sedimentary type sulfide deposit. The Co/Ni ratios in pyrite from carbonaceous phyllite and banded impure marble are less than 1. This ratio also suggests the sedimentary origin of the sulfides. These pyrite

grains show biogenic texture. In this belt, typical red beds and evaporite sequence associated with sedimentary sulfide deposit are missing.

Epigenetic hydrothermal mode is defined by the presence of copper mineralization in the form of facture filling, vein filling, semi-massive and fine dissemination of bornite, chalcopyrite, chalcocite, pyrite, and pyrrhotite. Mutual grain contact between sulfide phases indicates that they all formed due to the same fluid. Fracture and vein filling nature of bornite and chalcopyrite indicates the hydrothermal fluid activity. The Co/Ni ratios in pyrite and pyrrhotite in banded impure marble are greater than 1. That indicates the hydrothermal origin of the pyrite and pyrrhotite. These pyrite and pyrrhotite are associated with the copper ore body. Low Ti and Al concentration in magnetite indicate the presence of hydrothermal fluid in ore system. Homogenization temperature of 110 °C to 391 °C in quartz vein indicates hydrothermal condition of ore deposits. The sulfur isotopic data of copper sulfides indicate the hydrothermal origin of metal source. Hydrothermal barites generally have $\delta^{34}S$ values in between 1.5 and 20‰ (Stadue et al. 2011). In NKTCB, copper sulfide–bearing barite veins were analyzed by Sharma et al. 2020 and shows $\delta^{34}S$ values from 16.14 to 20.12‰. This data indicate the presence of hydrothermal fluid in the system and that associated with the copper mineralization in the area. Ore mineral textures

**Fig. 14** The sulfur isotopic composition of Nim Ka Thana Copper Belt with the some geological important sulfur reservoirs and some important copper deposits worldwide. The sulfur isotopic composition of Cheliean and Iranian Manto type data from Maghfouri et al.,2016; IOCG and Indian deposits data from Dora et al., 2019; Sediment hosted Cu deposits from Vaughan et al. (1989) and McGowan et al. (2006); Porphyry copper deposit from Field and Gustafson (1976) and Wanhainen et al. (2006)
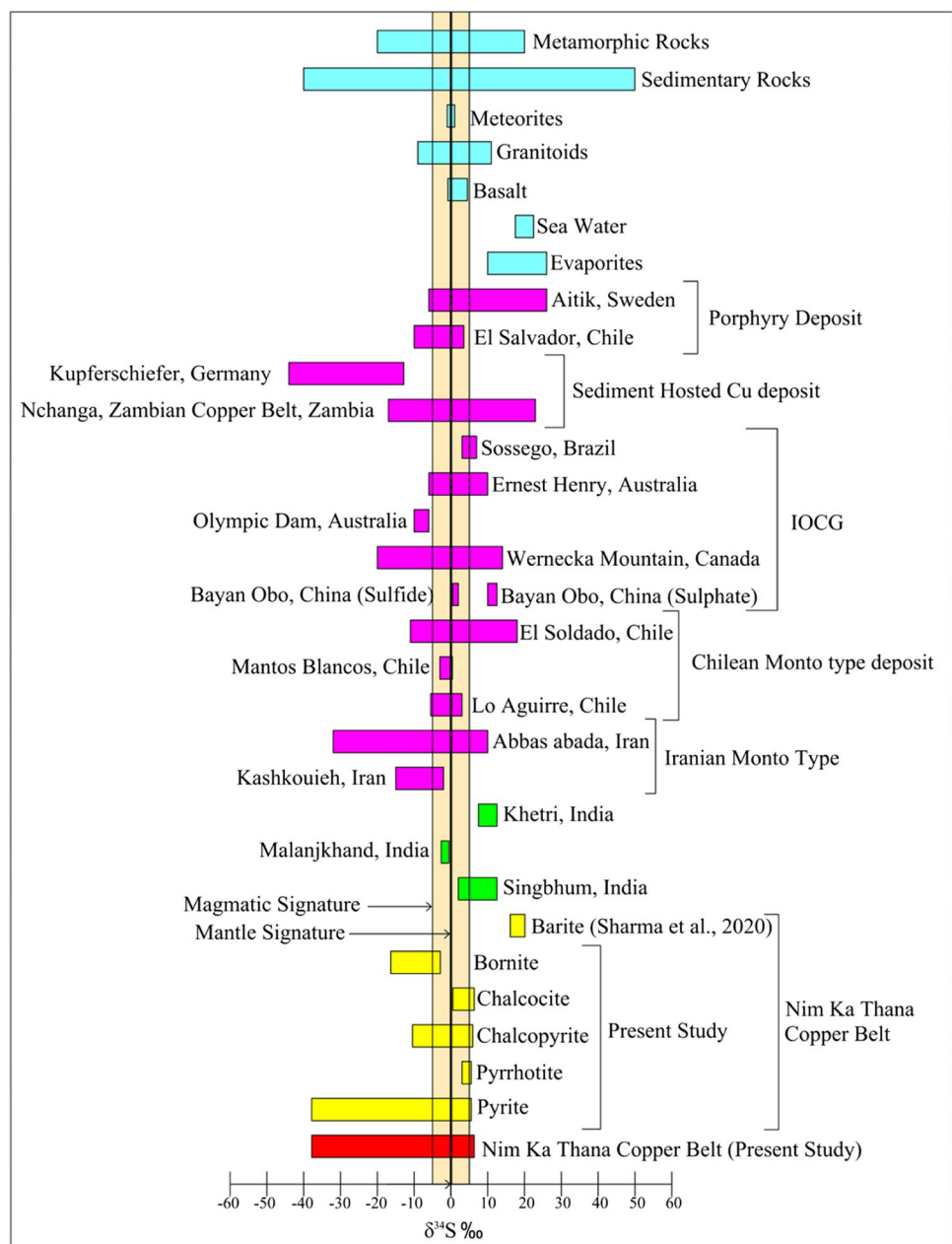


such as replacement and straight grain boundary indicate the hydrothermal environment. Epigenetic hydrothermal model also supported by the presence of scapolitization and amphibolization.

## Conclusions

Based on the present study on Nim Ka Thana Copper Belt, it is inferred that:

1. The copper mineralization in Nim Ka Thana Copper Belt is hosted within a Paleoproterozoic hydrothermally altered bended impure marble.
2. Hydrothermal alteration is dominated by Ca-Na–K-B metasomatism represented by scapolitization, amphibolization, biotitization, and tourmalization occurring in the close proximity to copper ore body.
3. Co/Ni ratio in pyrite and pyrrhotite indicates two different styles of sulfide mineralization one is sedimentary and other is hydrothermal. Low concentration of Ti and Al in magnetite indicates presence of hydrothermal fluid in ore system.

4. Three types of fluid inclusions observed within the mineralized quartz veins. The homogenization temperature ranges from 110 to 391 °C and salinity varying from 0.33 to 16.80 wt% NaCl equivalent. This data indicate that the ore-forming fluids were characterized by medium to high temperature and medium to low salinity and $H_2O$-$CO_2$-NaCl system, isothermal mixing and simple cooling with boiling occurred during the mineralization process.

5. Fluid inclusion microthermometry and sulfur isotopic composition indicates that the ore fluids were evolved from the mixture of magmatic and non-magmatic fluid source. The non-magmatic fluid source was metamorphic fluids which generates during the second phases of deformation.

6. The sulfur isotopic data of NKTCB indicates bimodal distribution and divided into two classes. Class-I ranges from $-16.32‰$ to $+6.33‰$ that indicates hydrothermal origin of sulfur and class-II ranges from $-37.85‰$ to $-32.63‰$ that indicates biogenic/ sedimentary origin of sulfur.

7. Geology, mineral chemistry, ore and gangue mineral association, hydrothermal alteration, fluid inclusions, and sulfur isotope systematic indicate that sulfide mineralization in NKTCB is formed by sedimentary and hydrothermal processes. Copper mineralization is mainly hydrothermal type and late phase remobilization.

**Data availability** I declared that the work is original and the data which generate during the work is original. Whenever materials (data, theoretical analysis, and text) from other sources have been used, credit has been given to them in the text of the report and their details in the references.

## Declarations

**Competing interest** The authors declare no competing interest.

## References

Ahmad T, Dragusanu C, Tanaka T (2008) Provenance of Proterozoic Basal Aravalli mafic volcanic rocks from Rajasthan, Northwestern India: Nd isotopes evidence for enriched mantle reservoirs. Precambrian Res 162:150–159. https://doi.org/10.1016/j.precamres.2007.07.011

Anand A (2019) Ore genesis and isotopic studies of sulphide mineralization of Dariba North Block, Sikar district, Rajasthan. Unpubl. Rep. Geol. Surv. India

Asthana D, Kumar H, Balakrishnan S, Xia Q, Feng M (2015) An early cretaceous analog of the 2.5 Ga Malanjkhand porphyry Cu deposit Central India. Ore Geol Rev 72:1197–1212. https://doi.org/10.1016/j.oregeorev.2015.10.015

Audétat A, Edmonds M (2020) Magmatic—hydrothermal fluids. Elements 16(6):401–406. https://doi.org/10.2138/gselements.16.6.401

Ault KM, Williams-Jones AE (2004) Sulfur and lead isotope study of the EL Mochito Zn-Pb-Ag deposit. Econ Geol 99:1223–1231. https://doi.org/10.2113/gsecongeo.99.6.1223

Baidya AS, Paul J, Pal DC, Upadhyay D (2017) Mode of occurrences and geochemistry of amphibole in the Kolihan-Chandmari copper deposits, Rajasthan, India: insight into the ore forming process. Ore Geol Rev 80:1092–1110. https://doi.org/10.1016/j.oregeorev.2016.08.032

Baidya AS, Pal DC (2020) Geochemical evolution and timing of uranium mineralization in the Khetri Copper Belt, western India. Ore Geol. Rev. 127:103794. https://doi.org/10.1016/j.oregeorev.2020.103794

Bajwah ZU, Seccombe PK, Offler R (1987) Trace element distribution, Co/Ni ratios and genesis of the Big Cadia iron-copper deposit, New South Wales Australia. Miner Depos 22:292–300. https://doi.org/10.1007/BF00204522

Baker T, Bertelli M, Blenkinsop T, Cleverley JS, Mvlellan J, Nugus M, Gillen D (2010) P-T-X conditions of fluids in the Sunrise Dam gold deposit, Western Australia, and implications for the interplay between deformation and fluids. Econ Geol 105:873–894. https://doi.org/10.2113/econgeo.105.5.873

Beaudoin G, Taylor BE (1994) High precision and spatial resolution sulfur isotope analysis using MILES laser microprobe. Geochim Cosmochim Acta 58(22):5055–5063. https://doi.org/10.1016/0016-7037(94)90231-3

Bhargava M, Pal AB (2000) Cu-Mo-Au metallogeny associated with Proterozoic tectonomagmatism in Malanjkhand Porphyry copper district Madhya Pradesh. J Geol Soc India 56:395–413

Bhattacharya HN, Bull S (2010) Tectono-sedimentary setting of the Paleoproterozoic Zawar Pb–Zn deposits, Rajasthan India. Precambrian Res 177:323–338. https://doi.org/10.1016/j.precamres.2010.01.004

Biju-Sekhar S, Yokoyama K, Pandit MK, Okudaira T, Yoshida M, Santosh M (2003) Late Paleoproterozoic magmatism in Delhi Fold Belt, NW India and its implication: Evidence from EPMA chemical ages of zircons. J Asian Earth Sci 22:189–207. https://doi.org/10.1016/S1367-9120(02)00188-8

Bodnar RJ (1983) A method of calculating fluid-inclusion volumes based on vapor bubble diameters and P-V-T-X properties of inclusion fluids. Econ Geol 78:535–542. https://doi.org/10.2113/gsecongeo.78.3.535

Bodnar RJ, Binns PR, Hall DL (1989) Synthetic fluid inclusions—VI. Quantitative evaluation of the decrepitation behavior of fluid inclusions in quartz at one atmosphere confining pressure. J Metamorph Geol 7:229–242. https://doi.org/10.1111/j.1525-1314.1989.tb00586.x

Bodnar RJ (1993) Revised equation and table for determining the freezing point depression of $H_2O$–NaCl solutions. Geochim Cosmochim Acta 57:683–684. https://doi.org/10.1016/0016-7037(93)90378-A

Bodnar RJ, Lecumberri-Sanchez P, Moncada D, Steele-MacInnis M (2014) Fluid inclusions in hydrothermal ore deposits. In: Holland, H.D., Turekian, K.K. (Eds.), Treatise on Geochemistry, Second ed. Elsevier, Oxford, pp. 119–142

Borg G, Piestrzyñski A, Bachmann G, Püttmann W, Walther S, Fiedler M (2012) An Overview of the European Kupferschiefer Deposits. Econ Geol Spec Publ 16:455–486. https://doi.org/10.5382/SP.16.18

Bralia A, Sabatini G, Troja F (1979) A revaluation of the Co/Ni ratio in pyrite as geochemical tool in ore genesis problems. Miner Deposita 14:353–374. https://doi.org/10.1007/BF00206365

Brown PE, Lamb WM (1989) P-V-T properties of fluids in the system H2O-CO2-NaCl: new graphical presentation and implications for fluid inclusion studies. Geochim Cosmochim Acta 53:1209–1221. https://doi.org/10.1016/0016-7037(89)90057-4

Chen WT, Mei-Fu Z, Li X, Jian-Feng G, Hou K (2015) In-situ LA-ICP-MS trace elemental analyses of magnetite: Cu-(Au, Fe) deposits in the Khetri copper belt in Rajasthan Province NW India. Ore Geol Rev 65:929–939. https://doi.org/10.1016/j.oregeorev.2014.09.035

Choudhary AK, Gopalan K, Sastry CA (1984) Present status of the geochronology of the Precambrian rocks of Rajasthan. Tectonophys 105:131–140. https://doi.org/10.1016/0040-1951(84)90199-9

Chowdhury S, Pal DC, Papineau D, Lentz DR (2020) Major and trace element and multiple sulfur isotope composition of sulfdes from the Paleoproterozoic Surda copper deposit, Singhbhum shear Zone, India: implications for the mineralization processes. Ore Geol. Rev. 120:103396. https://doi.org/10.1016/j.oregeorev.2020.103396

Clark C, Grguric B, Mumm AS (2004) Genetic implications of pyrite chemistry from the Paleoproterozoic Olary Domain and overlying Neoproterozoic Adelaidean sequences, northeastern South Australia. Ore Geol Rev 25:237–257. https://doi.org/10.1016/j.oregeorev.2004.04.003

Cook NJ, Ciobanu CL, Mao J (2009) Textural control on gold distribution in As-free pyrite from the Dongping, Huangtuliang and Hougou gold deposits, North China Craton (Hebei Province, China). Chem Geol 264:101–121. https://doi.org/10.1016/j.chemgeo.2009.02.020

Cook NJ, Ciobanu CL, Danyushevsky LV, Gilbert S (2011) Minor and trace elements in bornite and associated Cu–(Fe)-sulfides: A LA-ICP-MS study. Geochim Cosmochim Acta 75:6473–6496. https://doi.org/10.1016/j.gca.2011.08.021

Craig JR, Vokes FM, Solberg TN (1998) Pyrite: physical and chemical textures. Miner Deposita 34:82–101. https://doi.org/10.1007/s001260050187

Dare SAS, Barnes SJ, Beaudoin G (2012) Variation in trace element content of magnetite crystallized from a fractionating sulfide liquid, Sudbury, Canada: implications for provenance discrimination. Geochim Cosmochim Acta 88:27–50. https://doi.org/10.1016/j.gca.2012.04.032

Dare SAS, Bames SJ, Beaudoin G, Meric J, Boutroy E, Potvin-Doucet C (2014) Trace elements in magnetite as petrogenetic indicators. Miner Deposita 49:785–796. https://doi.org/10.1007/s00126-014-0529-0

De Groot PA (2009) Handbook of stable isotope analytical techniques, vol.2, Elsevier, Amsterdam, pp.1372

Debnath S, Dewangan S, Javaid AZ (2017) General exploration for basemetal mineralization in Toda-Ramliyas Block, Sikar district, Rajasthan, UNFC-G2 stage. Unpubl. Rep. Geol. Surv. India

Dill HG (2015) Supergene alteration of ore deposits: from nature to humans. Elements 11:311–316. https://doi.org/10.2113/gselements.11.5.311

Dora M L, Upadhyay D, Randive K R, Shareef M, Baswani S R, Ranjan S (2020) Trace element geochemistry of magnetite and pyrite and sulfur isotope geochemistry of pyrite and barite from the Thanewasna Cu-(Au) deposit, western Bastar Craton, central India: Implication for ore genesis, Ore Geo Rev. 117: 103262. https://doi.org/10.1016/j.oregeorev.2019.103262.

Drüppel K, Wagner T, Boyce AJ (2006) Evolution of sulphide mineralization in ferrocarbonatite, Swartbooisdrif, Northwestern Namibia: constraints from mineral compositions and sulfur isotopes. Can Mineral 44:877–894. https://doi.org/10.2113/gscanmin.44.4.877

Dupuis C, Beaudoin G (2011) Discriminant diagrams for iron oxide trace element fingerprinting of mineral deposit types. Mineral Deposita 46:319–335. https://doi.org/10.1007/s00126-011-0334-y

Fareeduddin, Banerjee DM (2019) Aravalli Craton and its mobile belts: an update. Episodes 43(1):88–108. https://doi.org/10.18814/epiiugs/2020/020005

Field CW, Gustafson LB (1976) Sulfur isotopes in the porphyry copper deposit at El Salvador. Chile Econ Geol 71(8):1533–1548. https://doi.org/10.2113/gsecongeo.71.8.1533

Gantait A, Jakhar S, Nevin CG, Chauhan A (2018) General exploration for copper and associated metals in Dariba North Block, Sikar district, Rajasthan. Unpubl. Rep. Geol. Surv. India

Gehrig M, Lentz H, Franck EU (1979) Thermodynamic properties of water–carbon dioxide–sodium chloride mixtures at high temperatures and pressures. In: Timmerhaus, K.D., Barber, M.S. Eds., High Pressure Science and Technology. Physical Properties and Material Synthesis, vol. 1, pp. 539–542

Golani PR, Pandit MK, Sial A, Fallick AE, Ferreira VP, Roy AB (2002) B-Na rich Paleoproterozoic Aravalli metsediments of evaporitic association, NW India: a new repository of gold mineralization. Precamb Res 116:183–198. https://doi.org/10.1016/S0301-9268(02)00020-7

Goldstein RH, Reynolds TJ (1994) Systematics of fluid inclusions in diagenetic minerals. SEPM Short Course Notes 31:1–199

Gopalan K, Macdougall J, Roy A, Murali A (1990) Sm-Nd evidence for 3.3 Ga old rocks in Rajasthan, northwestern India. Precamb Res 48:287–297. https://doi.org/10.1016/0301-9268(90)90013-G

Groves DI, Bierlein FP, Meinert LD, Hitzman MW (2010) Iron oxide copper-gold (IOCG) deposits through Earth history: implications for origin, lithospheric setting, and distinction from other epigenetic iron oxide deposits. Econ Geol 105(3):641–654. https://doi.org/10.2113/gsecongeo.105.3.641

Gupta BC (1934) The Geology of Central Mewar; Geol. Surv India Memoir 65:07–168

Gupta P, Guha DB, Chattopadhyay B (1998) Basement-cover relationship in the Khetri Copper Belt and the emplacement mechanism of the granite massifs Rajasthan. J Geol Soc India 52:417–432

Hedenquist JW, Lowenstern JB (1994) The role of magmas in the formation of hydrothermal ore deposits. Nature 370:519–527. https://doi.org/10.1038/370519a0

Hedenquist JW, Richards JP (1998) The influence of geochemical techniques on the development of genetic models for porphyry copper deposits. Rev Econ Geol 10:235–256. https://doi.org/10.5382/Rev.10.10

Heinrich CA (2007) Fluid-fluid interactions in magmatic-hydrothermal ore formation. Rev Mineral Geochem 65:363–387. https://doi.org/10.2138/rmg.2007.65.11

Henley RW, Berger BR (2013) Nature's refneries—metals and metalloids in arc volcanoes. Earth-Sci Rev 125:146–170. https://doi.org/10.1016/j.earscirev.2013.07.007

Heron AM (1953) The geology of central Rajputana. Mem Geol Surv India 78:389

Hitzman MW (2000) Iron oxide-Cu-Au deposits: What, where, when, and why, in Porter, T.M., ed., Hydrothermal iron oxide copper-gold and related deposits: a global perspective: Adelaide, Australian Mineral Foundation 1:9–25

Hitzman M, Kirkham R, Broughton D, Thorson J, Selley D (2005) The sediment-hosted stratiform copper ore system. Econ Geol 100:609–642. https://doi.org/10.5382/AV100.19

Hitzman MW, Selley D, Bull S (2010) Formation of sedimentary rock-hosted stratiform copper deposits through Earth history. Econ Geol 105:627–639. https://doi.org/10.2113/gsecongeo.105.3.627

Hoefs J (2009) Stable Isotope Geochemistry, Springer-Verlag, Berlin, 288pp

Hou ZQ, Zaw K, Rona P (2008) Geology, fluid inclusions, and oxygen isotope geochemistry of the Baiyinchang pipe-style volcanic-hosted massive sulfide Cu deposit in Gansu Province, Northwestern China. Econ Geol 103:269–292. https://doi.org/10.2113/gsecongeo.103.1.269

Hutchison W, Finch AA, Boyce AJ (2020) The sulfur isotope evolution of magmatic-hydrothermal fluids: insights into ore-forming processes. Geochim Cosmochim Acta 288:176–198. https://doi.org/10.1016/j.gca.2020.07.042

Kaur P, Chaudhri N, Raczek I, Kröner A, Hofmann AW (2007) Geochemistry, zircon ages and whole-rock Nd isotopic systematics for Palaeoproterozoic A-type granitoids in the northern part of the Delhi belt, Rajasthan, NW India: implications for late Palaeoproterozoic crustal evolution of the Aravalli craton. Geol Mag 144:361–378. https://doi.org/10.1017/S0016756806002950

Kaur P, Chaudhri N, Raczek I, Kröner A, Hofmann AW (2009) Record of 1.82 Ga Andean type continental arc magmatism in NE Rajasthan, India: insights from zircon and Sm–Nd ages, combined with Nd–Sr isotope geochemistry. Gondwana Res 16:56–71. https://doi.org/10.1016/j.gr.2009.03.009

Kaur P, Chaudhri N, Raczek I, Kröner A, Hofmann AW, Okrusch M (2011) Zircon ages of late Palaeoproterozoic (ca. 1.72–1.70 Ga) extension-related granitoids in NE Rajasthan, India: regional and tectonic significance. Gondwana Res 19:1040–1053. https://doi.org/10.1016/j.gr.2010.09.009

Kaur P, Zeh A, Chaudhri N, Eliyas N (2017) Two distinct sources of 1.73–1.70 Ga A-type granites from the northern Aravalli orogen, NW India: constraints from in situ zircon U-Pb ages and Lu-Hf isotopes. Gondwana Res 49:164–181. https://doi.org/10.1016/j.gr.2017.05.012

Kesler SE, Haynes PS, Creech MZ, Gorman JA (1986) Application of fluid inclusion and rock gas analysis in mineral exploration. J Geoch Explor 25:201–215. https://doi.org/10.1016/0375-6742(86)90014-2

Kesler SE (2005) Ore forming fluids. Elements 1:13–18. https://doi.org/10.2113/gselements.1.1.13

Knight J, Lowe J, Joy S, Cameron J, Merrillees J, Nag S, Dua G, Jhala K (2002) The Khetri copper belt, Rajasthan: iron oxide copper–gold terrain in the Proterozoic of NW India. In: Porter, T.M. (Ed.), Hydrothermal iron oxide Copper-Gold and related deposits: a global perspective V2. PGC Publishing, Adelaide, pp. 321–341

Kouzmanov K, Pokrovski GS (2012) Hydrothermal controls on metal distribution in porphyry Cu (-Mo-Au) Systems. Soc Econ Geol Inc Spec Publ 16:573–618. https://doi.org/10.5382/SP.16.22

Lal RK, Ackermand D (1981) Phase petrology and polyphase andalusite-sillimanite type regional metamorphism in pelitic schist of the area around Akwali, Khetri Copper Belt, Rajasthan, India. Neues Jahrbuch Für Mineralogie-Abhandlungen 141:161–185

Landtwing MR, Furrer C, Redmond PB, Pettke T, Guillong M, Heinrich CA (2010) The Bingham Canyon porphyry Cu-Mo-Au deposit. III. Zoned copper-gold ore deposition by magmatic vapor expansion. Econ Geol 105:91–118. https://doi.org/10.2113/gsecongeo.105.1.91

Lecumberri-Sanchez P, Steele-MacInnis M, Weis P, Driesner T, Bodnar RJ (2015) Salt precipitation in magmatic-hydrothermal systems associated with upper crustal plutons. Geology 43:1063–1066. https://doi.org/10.1130/G37163.1

Li XC, Zhou MF, Williams-Jones AE, Yang YH, Gao JF (2018) Timing and genesis of Cu-(Au) mineralization in the Khetri Copper Belt, Northwestern India: constraints from in Situ U-Pb Ages and Sm-Nd Isotopes of Monazite-(Ce). Mineral Depos 54:553–568. https://doi.org/10.1007/s00126-018-0823-3

Li K, Pring A, Etschmann B, Xia F, Brugger J (2019) Coupling between mineral replacement reactions and co-precipitation of trace elements: an example from the giant Olympic Dam deposit. Ore Geol. Rev. 117:103267. https://doi.org/10.1016/j.oregeorev.2019.103267

Liebscher A, Heinrich CA (2007) Fluid-Fluid Interactions in the Earth's Lithosphere. Rev Mineral Geochem 65:1–13. https://doi.org/10.2138/rmg.2007.65.1

Liu B, Li H, Wu Q-H, Kong H, Xi X-S (2019) Double-vein (ore-bearing vs. ore-free) structures in the Xitian ore field, South China: implications for fluid evolution and mineral exploration. Ore Geol. Rev. 115:103181. https://doi.org/10.1016/j.oregeorev.2019.103181

Maghfouri S, Hosseinzadeh MR, Moayyed M, Movahednia M, Choulet F (2017) Geology, mineralization and sulfur isotopes geochemistry of the Mari Cu (Ag) Manto-type deposit, northern Zanjan Iran. Ore Geo Rev 81(1):10–12. https://doi.org/10.1016/j.oregeorev.2016.10.025

Mathur R, Falck H, Belogub E, Milton J, Wilson M, Rose A, Powell W (2018) Origins of chalcocite defined by copper isotope values. Geofluids 2018:5854829. https://doi.org/10.1155/2018/5854829

Mathur R, Ruiz J, Casselman MJ, Megaw P, Egmond RV (2012) Use of Cu isotopes to distinguish primary and secondary Cu mineralization in the Cañariaco Norte porphyry copper deposit, Northern Peru. Miner Deposita 47:755–762. https://doi.org/10.1007/s00126-012-0439-y

McGowan RR, Roberts S, Boyce AJ (2006) Origin of the Nchanga copper–cobalt deposits of the Zambian Copper belt. Miner Deposita 40:617. https://doi.org/10.1007/s00126-005-0032-8

McKenzie NR, Hughes NC, Myrow PM, Banerjee DM, Deb M, Planavsky NJ (2013) New age constraints for the Proterozoic Aravalli-Delhi successions of India and their implications. Precambrian Res 238:120–128. https://doi.org/10.1016/j.precamres.2013.10.006

Mernagha TP, Leys C, Henley RW (2020) Fluid inclusion systematics in porphyry copper deposits: the super-giant Grasberg deposit, Indonesia, as a case study. Ore Geol. Rev. 123:103570. https://doi.org/10.1016/j.oregeorev.2020.103570

Mishra B, Pal N, Ghosh S (2003) Fluid Evolution of the Mosabani and Rakha Copper Deposits, Singhbhum District, Jharkhand: evidence from Fluid Inclusion Study of Mineralized Quartz Veins. J Geol Soc India 61:51–60

Moncada D, Mutchler S, Nieto A, Reynolds TJ, Rimstidt JD, Bodnar RJ (2012) Mineral textures and fluid inclusion petrography of the epithermal Ag–Au deposits at Guanajuato, Mexico: Application to exploration. J Geoch Explor 114:20–35. https://doi.org/10.1016/j.gexplo.2011.12.001

Mondal B, Debnath S, Dewangan S (2016) Report on exploration for basemetal in west of Nanagwas area, Sikar district, Rajasthan, UNFC-G2 stage. Unpubl. Rep. Geol. Surv. India

Mondal B, Debnath S, Dewangan S (2019) A significant find of a low grade copper resource of Nanagwas Block, Nim ka thana Copper Belt, Rajasthan: a promising future resource. J Geol Soc India 93(1):33–36. https://doi.org/10.1007/s12594-019-1117-9

Moon KJ (1991) Application of fluid inclusions in mineral exploration. J Geoch Explor 42:205–221. https://doi.org/10.1016/0375-6742(91)90068-6

Mukhopadhyay S (2014) Stratabound bornite dominated copper-silver mineralization in Baniwala Ki Dhani – Dokan – Panchokharkhara area in Mesoproterozoic Delhi Supergroup, northeast Rajasthan. Indian J Geosci 68(4):325–336

Mukhopadhyay S, Kumar V, Sangwan M (2019) Sediment hosted stratiform Copper (SSC) mineralization in Bhudoli-Basari Area, North Delhi Fold Belt, Mesoproterozoic Delhi Supergroup

Rajasthan. J Geol Soc India 93(6):663–674. https://doi.org/10.1007/s12594-019-1245-2

Nadoll P, Mauk JL, Hayes TS, Koenig AE, Box SE (2012) Geochemistry of magnetite from hydrothermal ore deposits and host rocks of Mesoproterozoic Belt Supergroup, United States. Econ Geol 107:1275–1292. https://doi.org/10.2113/econgeo.107.6.1275

Nadoll P, Angerer T, Mauk JL, French D, Walshe J (2014) The chemistry of hydrothermal magnetite: a review. Ore Geol Rev 61:1–32. https://doi.org/10.1016/j.oregeorev.2013.12.013

Naha K, Mukhopadhyay DK, Mohanty R (1988) Structural evolution of the rocks of the Delhi Group around Khetri, northeastern Rajasthan. In: Roy, A.B. (Ed.), Precambrian of the Aravalli Mountain, Rajasthan, India, Mem. Geol. Soc. India, no.7, pp. 207–245

Ni P, Pan JY, Huang B, Wang GG, Xiang HL, Yang YL, Li SN, Bao T (2018) Geology, ore-forming fluid and genesis of the Qiucun gold deposit: Implication for mineral exploration at Dehua prospecting region, SE China. J Geoch Explor 195:3–15. https://doi.org/10.1016/j.gexplo.2018.03.018

Ohmoto H (1972) Systematics of sulfur and carbon isotopes in hydrothermal ore deposits. Econ Geol 67:551–578. https://doi.org/10.2113/gsecongeo.67.5.551

Ohmoto H, Goldhaber MB (1997) Sulfur and carbon isotopes. J Wiley and Sons, pp. 517–611

Ohmoto H, Rye RO (1979) Isotopes of sulfur and carbon; John Wiley and Sons: New York, NY, USA.

Pal DC, Barton DB, Sarangi AK (2009) Deciphering a multistage history affecting U-Cu (-Fe) mineralization in the Singhbhum Shear Zone, eastern India, using pyrite textures and compositions in the Turamdih U-Cu (-Fe) deposit. Mineral Deposita 44:61–80. https://doi.org/10.1007/s00126-007-0165-z

Pal DC, Trumbull RB, Wiedenbeck M (2010) Chemical and boron isotope compositions of tourmaline from the Jaduguda U (-Cu-Fe) deposit, Singhbhum shear zone, India: implications for the sources and evolution of mineralizing fluids. Chem Geol 277:245–260. https://doi.org/10.1016/j.chemgeo.2010.08.008

Panigrahi MK, Pandit D, Naik RK (2009) Genesis of the granitoid affiliated Paleoproterozoic copper–molybdenum deposit at Malanjkhand: a review of status. In: Kumar, S. (Ed.), Magmatism, Tectonism and Mineralization. Macmillan Publisher, India, pp. 265–292

Patel S, Upadhyay D, Mishra B, Kumar A, Sarangi AK (2021) Multiple episodes of hydrothermal alteration and uranium mineralization in the Singhbhum Shear Zone, eastern India: constraints from chemical and boron isotope composition of tourmaline. Lithos 388–389:106084. https://doi.org/10.1016/j.lithos.2021.106084

Perello J, Cox D, Garamjav D, Sanjdorj S, Diakov S, Schissel D, Munkhbat T, Oyun G (2001) Oyu Tolgoi, Mongolia: Siluro-Devonian Porphyry Cu-Au-(Mo) and high-sulfidation Cu mineralization with a cretaceous chalcocite blanket. Econ Geol 96:1407–1428. https://doi.org/10.2113/gsecongeo.96.6.1407

Pichavant M, Ramboz C, Weisbrod A (1982) Fluid immiscibility in natural processes: Use and misuse of fluid inclusion data: I. phase equilibria analysis—a theoretical and geometrical approach. Chem Geol 37:29–48. https://doi.org/10.1016/0009-2541(82)90064-X

Ray G, Webster I (2007) Geology and chemistry of the low Ti magnetite-bearing Heff Cu-Au skarn and its associated plutonic rocks, Heffley Lake, south-central British Columbia. Explor Min Geol 16:159–186. https://doi.org/10.2113/gsemg.16.3-4.159

Raymond OL (1996) Pyrite composition and ore genesis in the Prince Lyell copper deposit, Mt Lyell mineral field, western Tasmania Australia. Ore Geol Rev 10:231–250. https://doi.org/10.1016/0169-1368(95)00025-9

Reich M, Vasconcelos PM (2015) Geological and economic significance of supergene metal deposits. Elements 11:305–310. https://doi.org/10.2113/gselements.11.5.305

Riciputi LR, Cole DR, Machel HG (1996) Sulfide formation in reservoir carbonates of the Devonian Nishu Formation, Alberta, Canada: an ion microprobe study. Geochim Cosmochim Acta 60:325–336. https://doi.org/10.1016/0016-7037(96)83133-4

Rieger AA, Marschik R, Diaz M, Holzl S, Chiaradia M, Akker B, Spangenberg JE (2010) The hypogene iron oxide Copper-Gold mineralization in the Mantoverde District, Northern Chile. Econ Geol 105:1271–1299. https://doi.org/10.2113/econgeo.105.7.1271

Roedder E (1984) Fluid Inclusions. Reviews in mineralogy, Min. Soc. America, 12, 644

Roedder E (1992) Fluid inclusion evidence for immiscibility in magmatic differentiation. Geochim Cosmochim Acta 56:5–20. https://doi.org/10.1016/0016-7037(92)90113-W

Rollinson HR (1993) Using geochemical data: evaluation, presentation, interpretation, Longman, London

Roy AB (1988) Stratigraphic and tectonic framework of the Aravalli Mountain Range. Mem Geol Soc India 7:3–31

Roy AB, Sharma BL, Paliwal BS, Chauhan NK, Nagori DK, Golani PR, Bejarniya BR, Bhu H, Ali Sabah M (1993) Lithostratigraphy and tectonic evolution of the Aravalli Supergroup: a protogeosynclinal sequence. In: Casshyap, S.M. (Ed.), Rift Basins and Aulacogens. Gyanodaya Prakashan, Naini Tal, pp. 73–90

Roy AB, Kröner A (1996) Single zircon evaporation ages constraining the growth of the Archaean Aravalli craton, northwestern Indian Shield. Geol Mag 133:333–342. https://doi.org/10.1017/S0016756800009067

Roy AB, Jakhar SR (2002) Geology of Rajasthan–Precambrian to Recent; Scientific Publication (India), Jodhpur, 421p

Roy AB, Kröner A, Rathore S, Laul V, Purohit R (2012) Tectono-metamorphic and geochronologic studies from Sandmata Complex, northwest Indian Shield: implications on exhumation of Late-Palaeoproterozoic granulites in an Archaeanearly Palaeoproterozoic granite-gneiss terrane. J Geol Soc India 79:323–334. https://doi.org/10.1007/s12594-012-0053-8

Salama W, Gazley MF, Bonnett LC (2016) Geochemical exploration for supergene copper oxide deposits, Mount Isa Inlier, NW Queensland Australia. J Geoch Explor 168:72–102. https://doi.org/10.1016/j.gexplo.2016.05.008

Sarkar SC, Dasgupta S (1980) Geologic setting, genesis and transformation of sulfide deposits in the northern part of Khetri copper belt, Rajasthan, India—an outline. Miner Depos 15:117–137. https://doi.org/10.1007/BF00206508

Seal RR (2006) Sulfur Isotope Geochemistry of Sulfide Minerals. Rev Mineral Geochem 61:633–677. https://doi.org/10.2138/rmg.2006.61.12

Sharma JP, Sahoo PR, Mahanta H, Venkatesha AS, Babu EVSSK, John M (2020) Constraints on the genesis of the Proterozoic bornite dominated copper deposit from Nim ka Thana, western India: An IOCG perspective. Ore Geol Rev 118:1–17. https://doi.org/10.1016/j.oregeorev.2020.103338

Sharma RK, Sharma V, Khan I (2015) Geology and emplacement mechanism of the bornite-dominated Cu-Ag mineralization at Dariba-Baniwala ki Dhani-Dokan Belt. GSI spl pub, Sikar district Rajasthan, pp. 177–190

Sharma RK, Mondal B, Dewangan S, Debnath S (2018) A possible hypogene environment indicator of copper mineralisation in Neem Ka Thana Copper Belt, Sikar District, Rajasthan India. Indian J Geosci 72(4):283–290

Shepherd TJ, Rankin AH, Alderton DHM (1985) A practical guide to fluid inclusion studies, Blackie, Glasgow and London, pp.239

Sillitoe RH (2003) Iron oxide-copper-gold deposits: an Andean view. Miner Deposita 38:787–812. https://doi.org/10.1007/s00126-003-0379-7

Sillitoe RH (2010) Porphyry copper systems. Econ Geol 105:3–41. https://doi.org/10.2113/gsecongeo.105.1.3

Sillitoe RH (2012) Copper provinces. Soc. Econ. Geol. Publ. 16:1–18 https://doi.org/10.5382/SP.16.01https://doi.org/10.5382/SP.16.01

Sillitoe RH, Perelló J, Creaser RA, Wilton J, Wilson AJ, Dawborn T (2017) Age of the Zambian Copper belt. Mineral Depos 52:1245–1268. https://doi.org/10.1007/s00126-017-0726-8

Simmons SF, Brown KL (2006) Gold in magmatic hydrothermal solutions and the rapid formation of a giant ore deposit. Science 314:288–290. https://doi.org/10.1126/science.1132866

Simon AC, Ripley EM (2011) The Role of magmatic sulfur in the formation of ore deposits. Rev Mineral Geochem 73:513–578. https://doi.org/10.2138/rmg.2011.73.16

Sinclair WD (2007) Porphyry deposits, in Goodfellow, W.D., ed., Mineral deposits of Canada: a synthesis of major deposit-types, District Metallogeny, the Evolution of Geological Provinces, and Exploration Methods: Geological Association of Canada, Mineral Deposits Division, Special Publication No. 5, p. 223-243

Singh SP (1988) Stratigraphy and sedimentation pattern in the Proterozoic Delhi Supergroup Northwestern India. Mem Geol Soc India 7:193–206

Sinha-Roy S (1984) Precambrian crustal interaction in Rajasthan, NW India. In: Proceeding of Seminar on Crustal Evolution of Indian Shield and its Bearing on Metallogeny. pp. 84–91

Sinha-Roy S (2004) Proterozoic rifting and major unconformities in Rajasthan and their implications for uranium mineralization. Explor Res Atom Min 15:69–97

Skirrow RG, Bastrakov EN, Barovich K, Fraser GL, Creaser RA, Fanning CM, Raymond OL, Davidson GJ (2007) Timing of iron oxide Cu-Au-(U) hydrothermal activity and Nd isotope constraints on metal sources in the Gawler craton South Australia. Econ Geol 102(8):1441–1470. https://doi.org/10.2113/gsecongeo.102.8.1441

Staude S, Gob S, Pfaff K, Strobele F, Premo WR, Markl G (2011) Deciphering fluid sources of hydrothermal systems: a combined Sr- and S-isotope study on barite (Schwarzwald, SW Germany). Chem Geol 286:1–20. https://doi.org/10.1016/j.chemgeo.2011.04.009

Steele-MacInnis M, Manning CE (2020) Hydrothermal properties of geologic fluids. Elements 16(6):375–380. https://doi.org/10.2138/gselements.16.6.375

Stein HJ, Hannah JL, Zimmerman A, Markey RJ, Sarkar SC, Pal AB (2004) A 2.5 Ga porphyry Cu–Mo–Au deposit at Malanjkhand, central India: implications for Late Archean continental assembly. Precambrian Res 134:189–226. https://doi.org/10.1016/j.precamres.2004.05.012

Sun W, Jt W, Lp Z, Cc Z, Li H, Mx L, Ding X, Cy Li, Hy L (2017) The formation of porphyry copper deposits. Acta Geochimica 36:9–15. https://doi.org/10.1007/s11631-016-0132-4

Valencia VA, Eastoe C, Ruiz J, Ochoa-Landin L, Gehrels G, González-Leon C, Barra F, Espinoza E (2008) Hydrothermal evolution of the porphyry copper deposit at La Caridad, Sonora, Mexico, and the relationship with a neighboring high-sulfidation epithermal deposit. Econ Geol 103(3):473–491. https://doi.org/10.2113/gsecongeo.103.3.473

Van den kerkhof AM (1988) The system $CO_2$–$CH_4$–$N_2$ in fluid inclusions: theoretical modelling and geological applications. Ph.D. thesis, Vrije Universiteit Amsterdam, pp. 206

Van den kerkhof AM, Hein U F (2001) Fluid inclusion petrography. Lithos 55:27-47https://doi.org/10.1016/S0024-4937(00)00037-2

Vaughan DJ, Sweeney MA, Friedrich G, Diedel R, Haranczyk C (1989) The Kupferschiefer; an overview with an appraisal of the different types of mineralization. Econ Geol 84(5):1003–1027. https://doi.org/10.2113/gsecongeo.84.5.1003

Wanhainen C, Billström K, Martinsson O (2006) Age, petrology and geochemistry of the porphyritic Aitik intrusion, and its relation to the disseminated Aitik Cu-Au-Ag deposit, northern Sweden. GFF 128(4):273–286. https://doi.org/10.1080/11035890601284273

Wiedenbeck M, Goswami JN (1994) High-precision 207Pb/206Pb zircon geochronology using a small ion microprobe. Geochim Cosmochim Acta 58:2135–2141. https://doi.org/10.1016/0016-7037(94)90291-7

Wiedenbeck M, Goswami JN, Roy AB (1996) Stabilization of the Aravalli craton of northwestern India at 2.5 Ga: an ion microprobe zircon study. Chem Geol 129:325–340. https://doi.org/10.1016/0009-2541(95)00182-4

Wilkinson JJ (2001) Fluid inclusions in hydrothermal ore deposits. Lithos 55:229–272. https://doi.org/10.1016/S0024-4937(00)00047-5

Yf Xu, Ni P, Gg W, Jy P, Sj G, Chen H, Jy D, Li L (2016) Geology, fluid inclusion and stable isotope study of the Huangshan orogenic gold deposit: implications for future exploration along the Jiangshan-Shaoxing fault zone, South China. J Geoch Explor 171:37–54. https://doi.org/10.1016/j.gexplo.2016.02.004

Zhang QL, Ding TP (1989) Analysis of the reference material NBS-123 and the atomic weight of sulfur. Chinese Sci Bull 34:1086–1089

Zhao HX, Frimmel HE, Jiang SY, Dai BZ (2011) LA-ICP-MS trace element analysis of pyrite from the Xiaoqinling gold district, China: Implications for ore genesis. Ore Geol Rev 43:142–153. https://doi.org/10.1016/j.oregeorev.2011.07.006

Zhao J, Brugger J, Ngothai Y, Pring A (2014) The replacement of chalcopyrite by bornite under hydrothermal conditions. Am Miner 99:2389–2397. https://doi.org/10.2138/am-2014-4825

Zhu X, Wang J, Pang Z, Zhen S, Yang F, Xue J, Jia H, Shi G (2019) Ore geology, fluid inclusion microthermometry and H-O-S isotopes of the Liyuan gold deposit, Central Taihang Mountains North China. Craton Minerals 9:606. https://doi.org/10.3390/min9100606

Zhu YF, Zhou J, Zeng YS (2007) The Tianger (Bingdaban) shear zone hosted gold deposit, west Tianshan, NW China: petrographic and geochemical characteristics. Ore Geol Rev 32:337–365. https://doi.org/10.1016/j.oregeorev.2006.10.006